ANNUAL REVIEWS

Annual Review of Fluid Mechanics

Fluids at the Nanoscale: From Continuum to Subcontinuum Transport

Nikita Kavokine,[1] Roland R. Netz,[2] and Lydéric Bocquet[1]

[1]Laboratoire de Physique de l'École Normale Supérieure (LPENS), CNRS UMR 8023, ENS, Université PSL, Sorbonne Université, Université Paris-Diderot, Sorbonne Paris Cité, 75005 Paris, France; email: nikita.kavokine@ens.fr, lyderic.bocquet@ens.fr

[2]Fachbereich Physik, Freie Universität Berlin, Berlin 14195, Germany

Annu. Rev. Fluid Mech. 2021. 53:377–410

First published as a Review in Advance on October 5, 2020

The *Annual Review of Fluid Mechanics* is online at fluid.annualreviews.org

https://doi.org/10.1146/annurev-fluid-071320-095958

Keywords

nanofluidics, slippage, ion transport, subcontinuum, non-mean-field, statistical mechanics

Abstract

Nanofluidics has firmly established itself as a new field in fluid mechanics, as novel properties have been shown to emerge in fluids at the nanometric scale. Thanks to recent developments in fabrication technology, artificial nanofluidic systems are now being designed at the scale of biological nanopores. This ultimate step in scale reduction has pushed the development of new experimental techniques and new theoretical tools, bridging fluid mechanics, statistical mechanics, and condensed matter physics. This review is intended as a toolbox for fluids at the nanometer scale. After presenting the basic equations that govern fluid behavior in the continuum limit, we show how these equations break down and new properties emerge in molecular-scale confinement. A large number of analytical estimates and physical arguments are given to organize the results and different limits.

1. INTRODUCTION

Fluid flows at the nanometer scale have been studied indirectly in various disciplines for the last 50 years (Eijkel & van den Berg 2005). However, it is only 15 years ago that nanofluidics emerged as a field on its own, first as a natural extension of microfluidics toward smaller scales. Back then, it was an issue in itself to establish that nanofluidics deserves its own name, meaning that there are specific effects at the nanoscale that are not present at the microscale.

Indeed, the ultimate scale for observing specific effects is set by the molecular size of the fluid; more precisely, a critical confinement of $\ell_c = 1$ nm has generally been accepted as the limit of validity for the Navier–Stokes equation (Bocquet & Charlaix 2010, Sparreboom et al. 2010). Moreover, it is at the molecular scale that the fluidic functions of biological systems emerge: from the giant permeability and perfect selectivity of the aquaporin (Murata et al. 2000) to the ion specificity of KcsA (potassium channel of *Streptomyces* A) channels (MacKinnon 2004) and the mechano-sensitivity of Piezo channels (Wu et al. 2017), to name a few. However, 10 years ago, the exploration of this ultimate scale was hindered by technical challenges, as molecular-scale channels could not be fabricated artificially.

A decade later, nanofluidics has firmly established itself as a field (Bocquet 2020). Indeed, length scales associated with the electrostatics and the fluctuations of surfaces may reach up to several tens of nanometers, and their effects may be probed specifically in systems without molecular-scale confinement (Schoch et al. 2008, Bocquet & Charlaix 2010, Sparreboom et al. 2010). These length scales govern the key nanofluidic phenomena that have been demonstrated over the last 10 years, such as fast flows in carbon nanotubes (Holt et al. 2006), diffusio-osmotic energy conversion (Siria et al. 2013), and diode-type effects (Vlassiouk & Siwy 2007).

However, the progress in fabrication technology has now allowed researchers to overcome the challenges that have hindered the development of nanofluidics at the ultimate scales, and artificial devices with confinement down to about one water molecule in size (3 Å) have been achieved, in zero-dimensional (0D), 1D, or 2D geometry (Feng et al. 2016a, Gopinadhan et al. 2019, Tunuguntla et al. 2017). It is therefore an exciting time for nanofluidics, since it now has the potential to reverse-engineer biological functions: Minimal artificial systems that mimic biological processes may be designed and studied. Furthermore, nanofluidics is known for its short path from fundamental science to applications and innovation, and developments in single-channel fabrication are likely to have direct implications for filtration and membrane science (Bocquet 2020).

At this time of accelerated development of the field, one should realize that the nanoscales under study require new tools for understanding the physics at play. The need for "new physics" is particularly emphasized in a recent review by Faucher et al. (2019), who identified "critical knowledge gaps in mass transport through single-digit nanopores," that is, nanopores that are less than 10 nm in size. Those knowledge gaps exist largely because the tools applied for understanding the experiments are built on macroscopic fluid mechanics and continuum electrostatics. But consider now a typical nanochannel of one nanometer in radius. At physiological salt concentration, it contains only a single ion per 50-nm channel length. Similarly, the carbon nanotube porins studied by Tunuguntla et al. (2017) each contain about 30 water molecules. These numbers strongly suggest that discrete particle effects may be important and call for a statistical mechanics description. Furthermore, below 1-nm confinement, the length scales associated with the fluid dynamics become comparable to characteristic length scales of the electrons in the confining solids, such as the Thomas–Fermi length (Mahan 2000). This points to the necessity of describing the confining solids at the level of condensed matter physics, and not simply as a space impenetrable to the fluid molecules. Overall, understanding fluidic phenomena at the nanometer scales requires bridging the gap between fluid mechanics, statistical mechanics, and condensed matter physics.

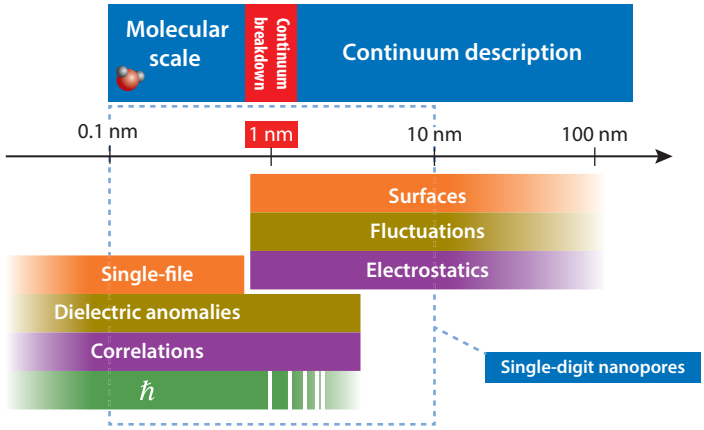

Figure 1

An overview of nanofluidic length scales: the main ingredients of the physics above and below the continuum limit.

In the past years, the breakdown of continuum equations has often set a hard limit for fluid mechanics: Below the continuum limit was the realm of molecular simulations. However, the need for understanding experiments has led to the development (or rediscovery) of analytical tools that have allowed researchers to identify some specific phenomena and associated length scales. The description of these phenomena is a key part of this review, as summarized in **Figure 1**. The review is organized as follows. In Section 2, we give a brief overview of available nanofluidic systems and fabrication methods. In Section 3, we focus on continuum modeling of nanofluidic systems, with particular emphasis on the precautions that should be taken when applying it to the smallest scales. Finally, in Section 4, we go below the continuum limit and highlight the specific phenomena that emerge along with the theoretical tools to describe them.

2. THE TOOLBOX OF EXPERIMENTAL SYSTEMS

Nanofluidics generally follows a bottom-up approach. Elementary phenomena are understood at the well-controlled scale of the individual channel, before eventually being applied to more complex systems. Hence, the design of these well-controlled systems is paramount to the development of the field. We start this review by going through the systems that have so far been achieved, in order of dimensionality.

2.1. Nanopores

Nanopores are channels whose length L and diameter d are both in the nanometer range (**Figure 2*a***). Initial studies focused on solid-state nanopores drilled through membranes made out of ceramics such as SiN (silicon nitride) or SiC (silicon carbide) (Dekker 2007, Keyser et al. 2006). More recently the advent of 2D materials, such as graphene, hBN (hexagonal boron nitride), or MoS_2 (molybdenum disulfide), allowed for the exploration of nanopores in atomically thin membranes (Garaj et al. 2010, Sahu & Zwolak 2019). Essentially three types of fabrication pathways have been reported for well-controlled nanopores in 2D materials.

2.1.1. Drilling with an electron or a focused ion beam. A single 5-nm-diameter pore drilled in monolayer graphene was first reported by Garaj et al. (2010). Celebi et al. (2014) reported

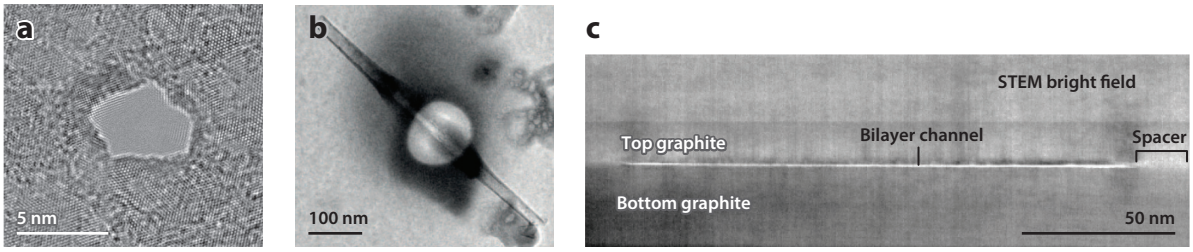

Figure 2

State-of-the-art nanofluidic systems of various dimensions. (*a*) Nanopore in single-layer MoS_2, drilled with a TEM (transmission electron microscope). (*b*) A boron nitride nanotube inserted into a SiN membrane. (*c*) STEM (scanning TEM) image of the nanoslit device fabricated by Radha et al. (2016). Panels adapted with permission from (*a*) Feng et al. (2016a), copyright 2016 Springer Nature; (*b*) Siria et al. (2013), copyright 2013 Springer Nature; and (*c*) Radha et al. (2016), copyright 2016 Springer Nature.

focused ion beam (FIB) drilling of arrays of nanopores in bilayer graphene, ranging from 7.6 nm to 1 μm in diameter.

2.1.2. Electrochemical etching. Feng et al. (2015) reported the opening of pores in monolayer MoS_2 when placed in a salt solution in between two electrodes. Applying a potential above the oxidation potential of MoS_2 resulted in the gradual removal of single MoS_2 units, thus creating an opening of controlled size. Nanopores down to 0.6 nm in diameter have been reported (Feng et al. 2016b).

2.1.3. Intrinsic defects in two-dimensional materials. Large-area membranes made of graphene or hBN are known to exhibit defects in the form of pores, ranging in size from a few angstroms to 15 nm depending on conditions (O'Hern et al. 2012, Walker et al. 2017); such defects may also be generated on purpose in smaller membranes using ultraviolet-induced oxidative etching (Koenig et al. 2012). The chemical vapor deposition (CVD) graphene membranes produced by Jain et al. (2015) exhibited pores in the sub-2-nm range spaced by 70 to 100 nm. Placing the membrane on top of a 30- to 40-nm pore of a SiN membrane allowed for the statistical isolation and study of a single pore.

2.2. Nanotubes

Nanotubes are cylindrical channels of diameter d in the nanometer range and length $L \gg d$ (**Figure 2*b***). They are typically made out of carbon or the isoelectronic boron nitride. The nanotubes themselves, as a product of self-assembly, are readily available, but interfacing a nanotube to a fluidic system and avoiding leakage are still experimental challenges. Three strategies for addressing this challenge have been reported.

2.2.1. Single-walled carbon nanotubes grown from chemical vapor deposition. Microfluidic systems may be built on top of one or more CVD-grown single-walled carbon nanotubes, typically of diameter 1 to 2 nm. The tubes generally have very high aspect ratio, with lengths up to 0.5 mm (Choi et al. 2013, Lee et al. 2010, Yazda et al. 2017), although similarly built systems with 20-μm-long nanotubes have also been reported (Pang et al. 2011).

2.2.2. Insertion of a multiwalled nanotube into a solid-state membrane. Siria et al. (2013) reported the fabrication of nanofluidic devices comprising a single boron nitride nanotube

inserted into a hole milled in a SiN membrane by direct nanomanipulation under a scanning electron microscope. The hole could be sealed in situ by cracking of naphthalene induced by the electron beam. The method was later extended by Secchi et al. (2016a) to carbon nanotubes of 30 to 100 nm in inner diameter and about 1 μm in length, and more recently to smaller, multiwall carbon nanotubes of 2 nm in inner diameter (Marcotte et al. 2020).

2.2.3. Insertion of nanotubes into a lipid membrane. Liu et al. (2013) reported the insertion of very short (5 to 10 nm in diameter) and very narrow (0.8 to 2 nm) nanotubes into a supported lipid membrane. Nanotubes were brought into contact with the lipid bilayer thanks to a microinjection probe. Recently, Tunuguntla et al. (2017) reported the self-assembly of similar (short and narrow) nanotubes, which they termed carbon nanotube porins, into phospholipid vesicles. A single patch of membrane could also be isolated in order to study a single porin.

2.3. Nanoslits Down to Angstrom Confinements

Slit-like channels with one dimension below tens of nanometers were first made using micro- and nanofabrication techniques. But recently, Radha et al. (2016) reported the manufacturing of 2D channels by van der Waals assembly of 2D materials (**Figure 2*c***). A few layers of graphene were used as spacers between two crystals of graphite, hBN, or MoS_2, allowing for atomically smooth channels of a few micrometers in length, 100 nm in width, and down to 7 Å in height, that is, the thickness of two graphene layers. More recently, Gopinadhan et al. (2019) reported the transport of water through channels that were one graphene layer thick (3.4 Å).

This brief overview highlights that nanofluidics at the molecular scale is now a reality. Not only is molecular-scale confinement possible, but the geometry of the confinement and the nature of the confining materials can also be tuned.

3. NANOFLUIDICS IN THE CONTINUUM LIMIT

3.1. Liquid Transport

We now embark on the discussion of theoretical tools used for the description of nanofluidic systems, with particular emphasis on their application to the smallest scales.

3.1.1. Basic equations. The two-centuries-old Navier–Stokes equation is remarkably robust at describing fluid flow down to the smallest scale, typically $\ell_c = 1$ nm for water in normal pressure and temperature conditions (Bocquet & Charlaix 2010). This length scale is essentially a lower bound for defining a fluid viscosity, η. Indeed, in macroscopic fluid mechanics, the kinematic viscosity $\nu = \eta/\rho$, where ρ is the mass density, plays the role of a diffusion coefficient for the fluid momentum. For such a diffusion coefficient to be defined, the time required for momentum to diffuse across the system, ℓ_c^2/ν, must be larger than the timescale of molecular motion, which is the microscopic origin of diffusion. A water molecule at a thermal agitation speed of 300 m/s moves by its own size in $\tau_c = 10^{-12}$ s, which defines a molecular timescale. Therefore, viscosity may be defined down to a system size:

$$\ell_c \sim \sqrt{\nu \tau_c} \sim 1\,\text{nm}. \qquad 1.$$

Below this length scale, water structuring due to surfaces, memory effects, and other subcontinuum phenomena come into play; these are discussed in Section 4. For water flow at 10-nm length scales, the Reynolds number remains smaller than 0.1 up to fluid velocities of 10 m/s. Hence, in

nanofluidic systems, inertial effects may be safely neglected, and the fluid flow is described by the Stokes equation:

$$\eta \Delta \mathbf{v} + \mathbf{f} = \nabla p, \qquad 2.$$

where p is the pressure and $\mathbf{f}$ is a body force, which may be due, for example, to the application of an electric field (see Section 3.3).

3.1.2. Boundary conditions. Stokes flow is often solved with no-slip boundary conditions: The velocity of the liquid is assumed to vanish at a solid–liquid interface. This is, however, a limiting case of the more general Navier partial-slip boundary condition, which enforces that the viscous stress at the interface should be balancing the solid liquid friction force per unit area. Within linear response theory, the friction force is proportional to the liquid velocity. For a fluid flowing in the direction x with slip velocity v_x along a surface of normal z, the force balance per unit area is $\sigma_{xz} = \lambda v_x$, with $[\sigma]$ the stress tensor and λ the friction coefficient per unit area (expressed in $\mathrm{N \cdot s/m^3}$). For a Newtonian fluid, we have $\sigma_{xz} = \eta \partial_z v_x$, which allows us to rewrite the Navier boundary condition as

$$v_x = b \left. \frac{\partial v_x}{\partial z} \right|_{\text{wall}}, \qquad 3.$$

introducing the slip length, $b = \eta/\lambda$. The slip length can be geometrically interpreted as the depth inside the solid where the linearly extrapolated fluid velocity profile vanishes. Accordingly, the no-slip boundary condition corresponds to $\lambda \to \infty$ or $b \to 0$. The effect of the partial-slip condition is to simply shift the no-slip velocity profile by the slip velocity, which is not negligible roughly within a slip length from the wall. Since slip lengths up to tens of nanometers have been measured on atomically flat (and hydrophobic) surfaces, slippage is expected to play a crucial role in nanofluidics (Bocquet & Barrat 2007, Lauga et al. 2007), and some of its effects will be discussed in the following sections. In the smallest channels, of size $R \ll b$, a perfect-slip boundary condition may even be appropriate: The flow is then controlled by entrance effects.

3.1.3. Geometry and entrance effects. Experimentally, the flow profile inside a nanofluidic channel can hardly be resolved, and one typically measures the total flow rate, Q. Under a pressure drop ΔP and no-slip boundary conditions, the flow rate through a cylindrical channel of radius R is given by the Hagen–Poiseuille formula:

$$Q_{\mathrm{c}} = \frac{\pi R^4}{8 \eta L} \Delta P. \qquad 4.$$

This formula assumes a channel length $L \gg R$, and thereby neglects the effect of channel mouths on the flow rate. But the transition from a macroscopic reservoir to a nanoscale channel is a source of viscous dissipation, as the streamlines need to be bent in order for the fluid to enter the channel. These entrance effects may be examined by considering the flow through an infinitely thin nanopore, which is of interest in itself, given the geometry of certain nanofluidic devices (see Section 2.1). This problem was addressed by Sampson (1891). For a nanopore of radius R (and vanishing length) under pressure drop ΔP, Sampson obtained the expression of the flow rate as

$$Q_{\mathrm{p}} = \frac{R^3}{3 \eta} \Delta P. \qquad 5.$$

The scaling in Sampson's formula naturally emerges from a Stokes equation where the only length scale is R: $\eta \Delta v = \nabla p \Rightarrow \eta v / R^2 \sim \Delta P / R$. The typical fluid velocity is $v \sim Q/R^2$. In order to estimate the flow rate through a channel by taking into account entrance effects, one may simply add the

hydrodynamic resistances of the pore ($\mathcal{R}_p$) and the channel ($\mathcal{R}_c$). If one writes $Q_c = (\Delta P)_c/\mathcal{R}_c$ and $Q_p = (\Delta P)_p/\mathcal{R}_p$, then the entrance-corrected flow rate Q_{pc} is obtained by imposing $Q_p = Q_c = Q_{pc}$ and $\Delta P = (\Delta P)_c + (\Delta P)_p$:

$$Q_{pc} = \frac{\Delta P}{\mathcal{R}_b + \mathcal{R}_p} = \frac{\pi R^4}{8\eta L}\frac{\Delta P}{1 + \frac{3\pi}{8}\frac{R}{L}}. \quad 6.$$

This result was first established by Weissberg (1962). An exact computation (Dagan et al. 1982) shows that the error made by this a priori crude approximation is less than 1%. Equation 6 makes a continuous transition between the nanopore and nanochannel regimes and shows that entrance effects are apparently negligible for channel lengths that exceed a few channel radii.

However, the above discussion has crucially not taken into account slippage, which, as we have highlighted in the previous section, is a strong effect at the nanoscale. Introducing a nonzero slip length b, the flow rate though a channel becomes

$$Q_c = \frac{\pi R^4}{8\eta L}\left(1 + \frac{4b}{R}\right)\Delta P, \quad 7.$$

while the flow rate through a pore is not significantly affected (Gravelle et al. 2013) since the source of dissipation in that case is mostly geometric. A full expression can be obtained by gathering previous results, but in the limit of $b \gg R$, the entrance-corrected flow rate becomes

$$Q_{pc} = \frac{R^3}{3\eta}\frac{\Delta P}{1 + \frac{2L}{3\pi b}}. \quad 8.$$

Thus, the hydrodynamic resistance is actually dominated by entrance effects as long as the channel is shorter than the slip length, rather than the channel radius (see **Figure 3*a***). In the presence of significant slippage, one should check whether the low–Reynolds number assumption still holds. The average velocity through a channel of radius $R = 5$ nm and length $L = 1\,\mu$m with slip length $b = 30$ nm under a pressure drop $\Delta P = 1$ bar is $v = 8$ mm/s, which is 25 times faster than the no-slip result but still well below the 10 m/s threshold established in Section 3.1.1.

Entrance-effect-dominated transport is particularly relevant for biological nanochannels, due to their relatively small aspect ratio. A striking example is aquaporin, which was recently studied

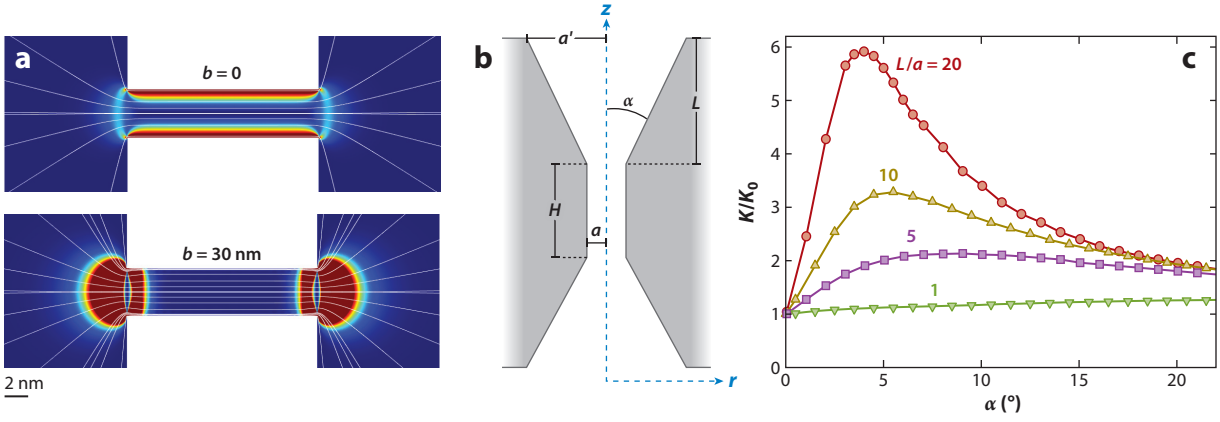

Figure 3

Entrance effects in nanofluidics. (*a*) Viscous dissipation rate, and streamlines, for the pressure-driven flow of water across a nanopore, as obtained from a finite-element solution of the Stokes equation (COMSOL) for two values of the slip length, *b*. The color scale, from blue to red, encodes the viscous dissipation. (*b*) Geometric model of the aquaporin as considered by Gravelle et al. (2013). (*c*) Normalized permeability, K/K_0, of the model aquaporin as a function of the cone angle, α.

from a hydrodynamic point of view by Gravelle et al. (2013). Aquaporins are channel proteins that selectively transport water across the cell membrane. A simplified geometrical model for the aquaporin consists of two conical vestibules connected by a sub-nanometric-diameter channel where water flows in single file (**Figure 3*b***). The single-file transport is expected to be nearly frictionless, and therefore the limit to the aquaporin's permeability is set by the entrance effects in the conical vestibules. Moreover, since the channel in question is less than 1 nm wide and slip lengths on the order of 10 nm are expected, perfect-slip boundary conditions are relevant for the flow, and the viscous dissipation has a purely geometric origin in the curvature of the stream lines. With the notation of **Figure 3*b***, Gravelle et al. (2013) expressed the total hydrodynamic resistance of the aquaporin as

$$R_{\mathrm{AQP}} = R_1 + R_2 = C_\infty \frac{\eta}{a'^3} + C_\infty \sin\alpha \frac{\eta}{a^3}. \qquad 9.$$

Both terms are the analogs of Sampson's formula (Equation 5): $C_\infty = 3.75$ replaces the factor 3 in the case of perfect-slip boundary conditions, and the factor $\sin\alpha$ appears because at the cone–cylinder transition, the stream lines turn by an angle α, as opposed to $\pi/2$ when the transition is from an infinite reservoir to a pore. With that, the permeability, $K = R_{\mathrm{AQP}}^{-1}$, turns out to be a nonmonotonic function of α (**Figure 3*c***), with the maximum permeability reached for cone angles in the range measured on aquaporin structures obtained by X-ray crystallography. It appears, therefore, that the geometry of the aquaporin is an optimum for hydrodynamic entrance effects, highlighting their particular relevance for nanoscale fluid transport.

3.2. Gas Transport

In a manner similar to liquid flow, gas flow can also be used to probe nanofluidic systems. Gas flow may display two limiting regimes, depending on the value of the Knudsen number, defined as

$$Kn = \frac{\ell}{R}, \qquad 10.$$

where ℓ is the mean free path and R is the typical system size. The mean free path scales as the inverse density according to $\ell \sim (\rho\sigma^2)^{-1}$, with σ the molecular diameter. For $Kn \ll 1$, the transport is dominated by intermolecular collisions and is therefore described by hydrodynamics, for example, by the Poiseuille or Sampson formula introduced above. For $Kn \gg 1$, the transport is dominated by collisions with the walls and is described by molecular diffusion: This is the so-called Knudsen regime (Lei et al. 2016). Consider a cylindrical channel of radius R and length $L \gg R$ connecting two gas reservoirs at pressures P_1 and P_2 and the same temperature, T (see **Figure 4*a***). One may then define a diffusion coefficient that relates the molecular flow rate Q_{K} to the density gradient $\Delta n/L$ across the channel through a Fick-type law:

$$\frac{Q_{\mathrm{K}}}{\pi R^2} = D_{\mathrm{K}} \frac{\Delta n}{L} = \frac{D_{\mathrm{K}}}{k_{\mathrm{B}} T} \frac{\Delta P}{L}. \qquad 11.$$

The last equality uses $n = P/k_{\mathrm{B}}T$ through the ideal gas law and $\Delta P = P_1 - P_2$. The only parameters involved in the diffusion are the channel radius R, the mean free path ℓ, and the average thermal velocity, $v^* = \sqrt{8k_{\mathrm{B}}T/\pi m}$, where m is the molecular mass of the gas. Since $\ell \gg R$, on dimensional grounds, the Knudsen diffusion coefficient should scale as $D_{\mathrm{K}} \sim Rv^*$. A kinetic theory computation (Knudsen 1909, Steckelmacher 1966) yields $D_{\mathrm{K}} = (2\pi/3)Rv^*$ and the Knudsen formula:

$$Q_{\mathrm{K}} = \frac{8}{3} \frac{\pi R^3}{\sqrt{2\pi m k_{\mathrm{B}} T}} \frac{\Delta P}{L}. \qquad 12.$$

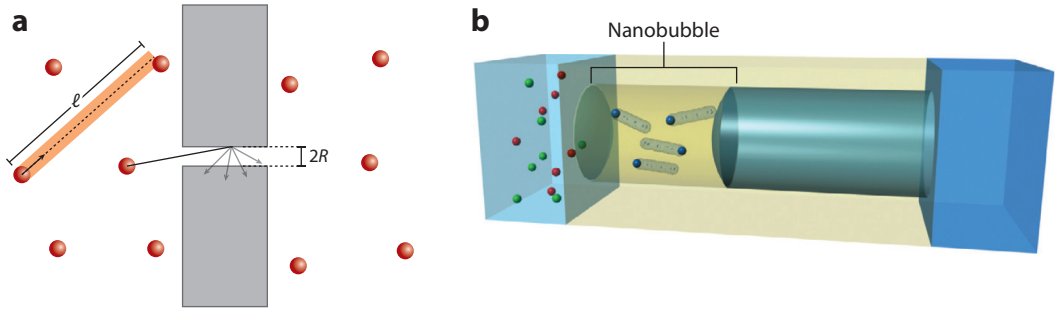

Figure 4

(*a*) Schematic of gas transport through a nanopore in the Knudsen regime, $\ell \gg R$. A diffuse reflection at the pore wall is represented. (*b*) Schematic of osmotic transport of water mediated by a nanobubble. Panel adapted with permission from J. Lee et al. (2014), copyright 2014 Springer Nature.

Now, the Knudsen formula relies on the crucial approximation of diffuse reflexion on the channel walls: A molecule that hits a wall has a new velocity randomly picked out of a Boltzmann distribution. It was proposed by Maxwell that only a fraction f of reflections should be diffuse, and the rest should be specular, that is, should correspond to elastic collisions. Smoluchowski then derived the corresponding correction to the Knudsen formula (Lei et al. 2016, Smoluchowski 1910):

$$Q_{\mathrm{K}} = \frac{2-f}{f} \cdot \frac{8}{3} \frac{\pi R^3}{\sqrt{2\pi m k_{\mathrm{B}} T}} \frac{\Delta P}{L}. \qquad 13.$$

There is a divergence of the flow rate in the limit $f \to 0$; that is, the channel opposes no more resistance to the gas flow when all the wall reflections are specular. This is to be expected, since in that case a molecule that enters the channel necessarily exits at the other end. The flow resistance is then dominated by entrance effects; in other words, the flow rate is given by the rate of molecules hitting the channel apertures. Gas molecules at a density n hit an aperture of area πR^2 at a rate $(1/4) n v^* \pi R^2$. Hence the effusion flow rate through an opening of radius R is

$$Q_{\mathrm{e}} = \pi R^2 \Delta n \sqrt{\frac{k_{\mathrm{B}} T}{2\pi m}} = \frac{\pi R^2}{\sqrt{2\pi m k_{\mathrm{B}} T}} \Delta P, \qquad 14.$$

which also sets the flow rate in a long channel with specular reflection at the walls. One notes there is a close analogy between the Poiseuille and Sampson formulae for liquids, on the one hand, and the Knudsen and effusion formulae for gases, on the other hand. The fraction of specular reflections $1-f$ plays a role similar to the slip length: If it is large, the transport in a long channel may still be dominated by entrance effects.

The free effusion prediction has been verified in systems of graphene nanopores (Celebi et al. 2014), with a transition to the hydrodynamic behavior (Sampson formula) observed upon reducing the Knudsen number. Specular reflections have also been evidenced in longer channels. Gas flow exceeding the Knudsen prediction was measured in carbon nanotubes (Holt et al. 2006, Majumder et al. 2008), and, recently, nearly ballistic transport was evidenced in angstrom-scale slits (Keerthi et al. 2018). These results point out that the tendency to anomalously fast transport in nanoscale confinement exists not only for liquids, but also for gases.

A striking example of gas-mediated osmotic flow was demonstrated by Karnik's group. J. Lee et al. (2014) fabricated a nanoporous (70-nm pore size) membrane with partially hydrophobic pores so that a nanobubble is trapped in each pore when the membrane is immersed in water (see **Figure 4*b***). The nanobubbles are impermeable to salt but permeable to water through its vapor-phase transport. They showed that the membrane reaches an ion rejection of 99.9%, while

competing with the permeability of state-of-the-art polyamide-based membranes. Such high permeability might seem counterintuitive since vapor-phase transport is expected to scale with the density of water vapor, which is 1,000 times lower than that of liquid water. However, using gas-phase transport as the ion rejection mechanism allows for much larger pores (70 nm) than what would be required in the liquid phase (~1 nm) to ensure steric rejection of ions. The scaling of the water transport rate with the pore size cubed (Bocquet 2014) then explains the high transport efficiency in the gas phase. As such, nanoscale gas transport shows promise for addressing the permeability–selectivity trade-off in membrane science.

3.3. Ion Transport

The behavior of ions in nanofluidic systems is of great practical interest, with applications ranging from biological ion channels (MacKinnon 2004) to ionic liquids inside nanoporous electrodes (Chmiola et al. 2006, Merlet et al. 2012). Ion transport also provides an indirect way of probing fluid transport, which is often useful, since electric currents are much easier to measure than fluid flow. However, due to their long-range Coulomb interactions and diffusive dynamics, ions in nanochannels give rise to physics of great complexity. In this section, we only sketch the main results with particular emphasis on how well-known equations apply to the smallest channels, and we refer the reader to other reviews on the subject (Bocquet & Charlaix 2010, Schoch et al. 2008, Sparreboom et al. 2010) for more details.

3.3.1. Basic equations. Consider an aqueous solution of monovalent salt. Let ρ_+ and ρ_- be the densities of positive and negative ions, respectively; D the diffusion coefficient, here assumed to be the same for ions of either sign; and ϕ the electrostatic potential. In a mean-field treatment, the convective-diffusive dynamics of ions are described by a Smoluchowski equation:

$$\frac{\partial \rho_\pm}{\partial t} = \nabla \cdot \left(D \nabla \rho_\pm \mp \frac{eD}{k_B T} (\nabla \phi) \rho_\pm + v \rho_\pm \right), \tag{15.}$$

where e is the unit charge and v is the fluid velocity field. The mean-field assumption implies, in particular, that correlations between the ions can be neglected; the potential importance of such correlations in nanofluidics is discussed in Section 4. Until then, we proceed by specifying the electrostatic potential through Poisson's equation:

$$\Delta \phi = -e \frac{\rho_+ - \rho_-}{\epsilon}, \tag{16.}$$

where ϵ is the dielectric permittivity of water. For now we assume it to be isotropic, although this assumption may break down for nano-confined water, as we discuss in Section 4. Lastly, we specify the flow velocity through the Stokes equation, which now includes an electrostatic term:

$$\eta \Delta v - e(\rho_+ - \rho_-) \nabla \phi = \nabla p. \tag{17.}$$

We now apply these three coupled equations to a specific geometry, although the discussion that follows could be generalized to channels of any shape. For simplicity, we consider a slit-like channel of height h, width w, and length L, with $w, L \gg h$, connecting two reservoirs of salt solution at concentration ρ_s. The channel extends along the direction x, between $z = 0$ and $z = h$. When considering ion transport, it is important to note that most surfaces are charged in water, due either to the dissociation of surface groups or to the adsorption of ions (Grosjean et al. 2019, Mouhat et al. 2020, Perram et al. 1973). Hence, we assume the channel wall carries a surface-charge density $-\Sigma e$ (Σ is expressed in elementary charges per unit area, and we assume here the surface charge to be negative).

3.3.2. Ionic conductance. We first neglect the coupling of ion transport to water transport, and consider the electrophoretic (EP) contribution to the ionic current under an applied electric field, E: This means that we start by setting the fluid velocity to $v = 0$. In the steady state, the Smoluchowski Equation 15 reduces to the so-called Nernst–Planck equations for the constant ionic fluxes (along the x-direction):

$$j_\pm = D\nabla_x \rho_\pm \mp \frac{eD}{k_B T}(\nabla_x \phi)\rho_\pm. \quad 18.$$

Together with the Poisson Equation 16, these constitute the widely used Poisson–Nernst–Planck (PNP) framework. In our geometry, the condition $L \gg h$ ensures $\nabla_x \rho_\pm = 0$ in the middle of the channel; moreover, to first order in E, we have $\nabla_x \phi = -E$ and the densities reduce to their equilibrium values. Hence, the EP contribution to the ionic current is

$$I_{ep} = w \int_0^h \mathrm{d}z(j_+ - j_-) = w\frac{e^2 D}{k_B T}\int_0^h \mathrm{d}z(\rho_+ + \rho_-)E. \quad 19.$$

In order to compute I_{ep}, one needs to find the equilibrium solution of the coupled PNP equations for ρ_+ and ρ_-. At equilibrium, $j_\pm = 0$ and the Nernst–Planck Equations 18 can be integrated, imposing $\phi = 0$ and $\rho_\pm = \rho_s$ in the reservoirs. This yields a Boltzmann distribution for the ions in the electrostatic potential:

$$\rho_\pm = \rho_s \exp\left(\mp\frac{e\phi}{k_B T}\right) \equiv \rho_s e^{\mp\psi}, \quad 20.$$

introducing a dimensionless potential ψ. Combining this with the Poisson Equation 16 yields the Poisson–Boltzmann equation (PB equation):

$$\Delta\psi - \lambda_D^{-2}\sinh(\psi) = 0, \quad 21.$$

which introduces the Debye length, $\lambda_D = (8\pi\rho_s \ell_B)^{-1/2}$, with $\ell_B = e^2/(4\pi\epsilon k_B T)$ the Bjerrum length. In our geometry, the PB equation has an implicit solution in terms of an elliptic integral (Andelman 1995, Levine et al. 1975). We do not exploit it here, however, and we instead recover the relevant limiting behaviors from qualitative considerations.

It is well known that, roughly speaking, the Debye length sets the extension of the diffuse layer of counterions next to a charged surface (Israelachvili 2011). Hence, if the channel height is $h \gg \lambda_D$, its two opposing walls do not see each other, so to speak. We expect the conductance to be the sum of a bulk term and a surface term originating in the two Debye layers:

$$I_{ep} = 2w\frac{e^2 D}{k_B T}E(\rho_s h + \Sigma). \quad 22.$$

where $\rho_s h$ and Σ account for the number of charge carriers in the bulk and at surfaces, respectively. In the opposite limit, $h \ll \lambda_D$, there is no more distinction between surface and bulk. All the quantities may be considered uniform across the channel: This is called the Debye overlap regime. However, one may not assume that the channel contains only counterions, and one should go back to the thermodynamic equilibrium with the reservoirs, which in this case is called the Donnan equilibrium (Bocquet & Charlaix 2010). One has $\rho_\pm = \rho_s e^{\mp\psi}$, which implies a chemical equilibrium, $\rho_+\rho_- = \rho_s^2$, in the channel. Going further, in the limit of long channel length, there should be local electroneutrality: $h(\rho_+ - \rho_-) = 2\Sigma$. This yields

$$\rho_\pm = \sqrt{\rho_s^2 + (\Sigma/h)^2} \pm \Sigma/h, \quad 23.$$

and the current–voltage relation in the Debye overlap regime is

$$I_{ep} = 2w\frac{e^2 D}{k_B T}E\sqrt{(\rho_s h)^2 + \Sigma^2}. \quad 24.$$

Debye length: $\lambda_D = (8\pi\rho_s \ell_B)^{-1/2}$; thickness of the diffuse layer of counterions next to a charged surface

Bjerrum length: $\ell_B = \frac{e^2}{4\pi\epsilon k_B T}$; distance between two unit charges at which their interaction energy is $k_B T$

Equation 24 displays the first peculiarity of small channels: One may not simply add the surface and bulk contributions. The table in the **Supplemental Appendix** lists the values of Debye length for different electrolyte concentrations, showing that the Debye overlap regime is indeed relevant for experimentally accessible nanofluidic systems (see Section 2). Qualitatively, Equations 22 and 24 both predict saturation of the conductance at low salt concentrations at a value determined by the surface charge. The saturation occurs for $\rho_s \sim \Sigma/h$, which can be recast in the form $\ell_{Du} \equiv \Sigma/\rho_s$. The so-called Dukhin length, ℓ_{Du}, quantifies the competition between bulk and surface contributions to the conductance. For a channel narrower than ℓ_{Du}, surface contributions dominate, and vice versa. The Dukhin length is important in our discussion below of entrance effects.

Dukhin length: $\ell_{Du} = \Sigma/\rho_s$; channel width below which surface conductance dominates over bulk conductance

Gouy–Chapman length: $\ell_{GC} = (2\pi\Sigma\ell_B)^{-1}$; distance a unit charge must travel from a charged surface so that its electrostatic energy is reduced by k_BT

At this point, a remark should be made concerning the range of validity of Equations 22 and 24. Indeed, they have been derived from qualitative considerations, without reference to the exact solution of the PB equation. Now, from Equations 19 and 20, one obtains more generally

$$I_{ep} = 2w\frac{e^2D}{k_BT}\left[\rho_s h\cosh(\psi(h/2)) + \frac{\mathcal{E}}{2k_BT}\right], \qquad 25.$$

where $\mathcal{E} = (\epsilon/2)\int_0^h(\partial_z\phi)^2 dz$ is the electrostatic energy per unit area. The electric double layer can be pictured as a capacitor with charge Σ; hence, one would expect its electrostatic energy to scale as Σ^2. Moreover, this is the prediction of the linearized PB equation, i.e., Equation 21 with the approximation $\sinh\psi \approx \psi$. This is in contrast to Equation 22, which predicts a linear scaling of the conductance with Σ: This scaling must therefore come from the nonlinearities of the PB equation. The PB equation may be linearized if the potential varies by less than k_BT across the Debye layer (or across the channel if there is Debye overlap). This is the case in the high-concentration/low-surface-charge limit and specifically when the Debye length is smaller than the so-called Gouy–Chapman length, $\ell_{GC} = (2\pi\Sigma\ell_B)^{-1}$. Thus, for Equation 22 to hold, one must be in the opposite limit, $\lambda_D \gg \ell_{GC}$, that is, high surface charge and low concentration. In practice, this condition is verified for most concentrations except for the highest (see the table in the **Supplemental Appendix**). In contrast, Equation 24, which is valid for the Debye overlap regime, is safe from a condition on ℓ_{GC}, as it predicts both quadratic and linear scalings depending on the value of Σ, as long as there is overlap of the Debye layers.

Supplemental Material >

3.3.3. Entrance effects. Similarly to what we have discussed for liquid and gas transport, we may now ask, for ion transport: What is the additional electrical resistance due to the channel–reservoir interface? Equivalently, we may want to estimate the ionic conductance of a nanopore of small aspect ratio, say of radius R and length $L \sim R$. The problem was first considered in the context of biological channels by Hille (1968) and Hall (1975). Hall solved the electrostatic problem with an electrode at infinity and an equipotential disk accounting for the entrance of the pore. Translating the solution into scaling arguments, we write the current through the pore entrance as $I \sim \pi R^2\kappa_b\Delta V_{out}/R$, where ΔV_{out} is the voltage drop at the entrance of the pore, which is expected to occur over a distance R and not over the macroscopic distance between the electrodes. This defines an electrical access resistance as the ratio $\Delta V_{out}/I$. We now specialize to the thin Debye layer regime, $\lambda_D \ll R$. If one simply sums the access resistance and the channel resistance as given by Equation 22 (adapted to cylindrical geometry), the current–voltage relation becomes

$$I_{ep} = \kappa_b\left(\frac{L}{\pi R^2}\frac{1}{1+\ell_{Du}/R} + \frac{1}{\alpha R}\right)^{-1}\Delta V, \qquad 26.$$

where α is a geometric factor that equals 2 in Hall's computation and $\kappa_b = 2e^2 D\rho_s/(k_B T)$ is the bulk conductivity. The above equation predicts vanishing conductance in the limit $\rho_s \to 0$, since the access resistance becomes infinite in this limit; however, this is not what is observed experimentally in short nanopores (Feng et al. 2016a, Lee et al. 2012). This inconsistency arises because, for a surface-charged pore, the access current has a surface contribution in addition to the bulk contribution.

This surface contribution may be evaluated starting from charge conservation at the surface, which imposes a relation between the axial and radial components of the electric field, as pointed out by Khair & Squires (2008),

$$\kappa_b E_r = \partial_x[\kappa_s \theta(x) E_x], \qquad 27.$$

where κ_s is the surface conductivity and θ is the Heaviside function, which accounts for the discontinuity of surface charge at the pore boundary. Equation 27 leads to subtle consequences: Indeed, it reveals that the Dukhin length, $\ell_{Du} = \Sigma/\rho_s \sim \kappa_s/\kappa_b$, is the relevant length scale for the surface contribution to the electric field outside the pore, instead of the channel radius or Debye length. The Dukhin length appears here as an electrostatic healing length: Feeding the surface conduction at the nanopore mouth disturbs the electric field lines in the bulk over a length ℓ_{Du}. This interpretation is supported by the numerical results of Lee et al. (2012), as shown in **Figure 5*a***.

The bending of the electric field lines can be estimated by a perturbative approach (Lee et al. 2012) that leads to an analytical expression for the corrected current–voltage relation:

$$I_{ep} = \kappa_b \left(\frac{L}{\pi R^2} \frac{1}{1 + \ell_{Du}/R} + \frac{1}{\alpha R + \beta \ell_{Du}} \right)^{-1} \Delta V. \qquad 28.$$

Bulk conductivity: κ_b relates the current density (in A/m^2) and the electric field in a bulk electrolyte: $\mathbf{j} = \kappa_b \mathbf{E}$

Surface conductivity: κ_s relates the surface current density (in A/m) to the electric field parallel to the surface: $\mathbf{j}_s = \kappa_s \mathbf{E}$

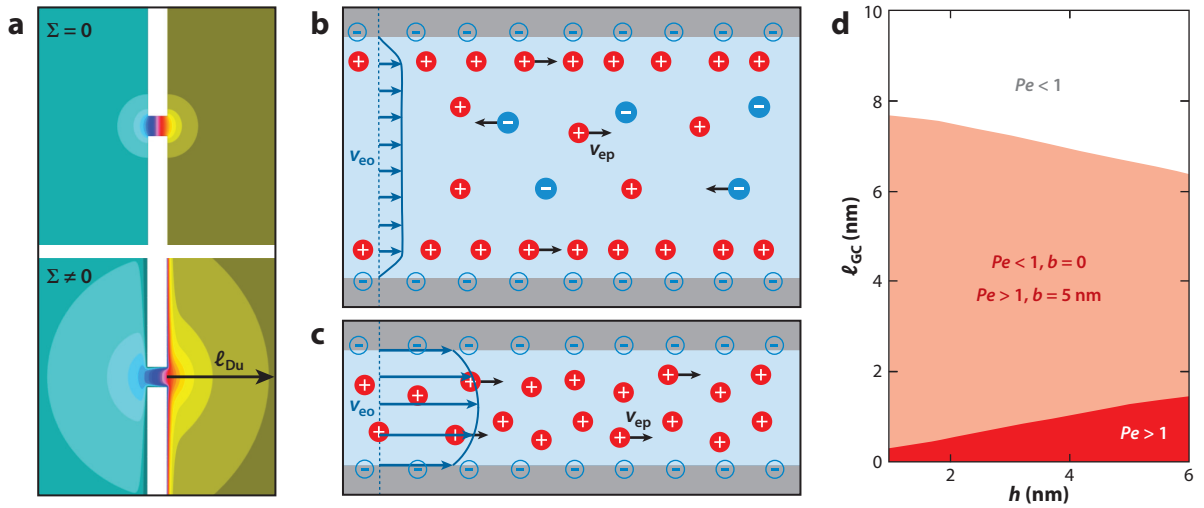

Figure 5

(*a*) Color plot of the electrostatic potential around a nanopore immersed in a salt solution and subject to a voltage drop, in the uncharged (*top*; $\Sigma = 0$) and in the charged case (*bottom*; $\Sigma \neq 0$). Around a charged pore, the length scale for variation of the potential is set by the Dukhin length ℓ_{Du}. Panel adapted with permission from Lee et al. (2012), copyright 2012 American Chemical Society. (*b*,*c*) Schematic representation of coupled ion and fluid transport in a nanochannel under electric field driving: in the thin–Debye layer limit (*b*) and in Debye overlap in the presence of slippage (*c*). The electro-osmotic velocity v_{eo} dominates the electrophoretic counterpart v_{ep} in the latter case. (*d*) Péclet number (defined in the text) as a function of channel width h and Gouy–Chapman length ℓ_{GC}. The region in parameter space with $Pe > 1$ is colored dark red in the no-slip case (slip length $b = 0$), and in light red when slippage is present.

The surface-charged pore therefore appears, from the perspective of entrance effects, as an uncharged pore of effective size $R + \ell_{Du}$, since the geometrical prefactor is $\beta \approx 2$. In the limit of vanishing salt concentration, $\rho_s \to 0$, the conductance indeed saturates, and, as expected, the entrance correction disappears in the limit of large–aspect ratio pores.

Lee et al. successfully compared the prediction of Equation 28 to experimental measurements in SiN nanopores in the range of 100–500 nm. More recently, Equation 28 has been used to describe conductance measurements in MoS_2 nanopores down to 2 nm in diameter (Feng et al. 2016a).

3.3.4. Coupling with fluid flow. So far, we have neglected any coupling of ion transport to fluid transport. However, in the presence of charged surfaces, an external electric field exerts a net force on the charged Debye layer, which sets the fluid in motion. This interfacially driven flow is termed electro-osmotic (EO) flow. The EO flow in turn drags along the ions in the Debye layer, which makes a supplementary contribution to the ionic current that we denote I_{eo}. This contribution has a convenient exact expression in the slit-like geometry considered in Section 3.3.2. In analogy to Equation 19, we have

$$I_{eo} = 2w \int_0^{h/2} e(\rho_+ - \rho_-) v(z)\, dz. \tag{29.}$$

From the Poisson Equation 16, we may replace $e(\rho_+ - \rho_-) = -\epsilon \partial_z^2 \phi$. Then, integrating by parts, we obtain

$$I_{eo} = 2w\epsilon \left[\int_0^{h/2} \partial_z \phi \partial_z v\, dz + v(0) \partial_z \phi|_0 \right]. \tag{30.}$$

Now, we may use the partial-slip boundary condition, $v(0) = b\partial_z v|_0$, as well as the electrostatic boundary condition, $\partial_z \phi|_0 = e\Sigma/\epsilon$. This stems from the Gauss theorem applied to the surface and the assumption that the medium outside the channel has much lower dielectric permittivity than water (Andelman 1995). Moreover, an integration of the Stokes Equation 17 allows for the replacement $\partial_z v = -(\epsilon E/\eta)\partial_z \phi$. Altogether, we obtain

$$I_{eo} = w \left[\frac{2\epsilon}{\eta} \mathcal{E} + \frac{2be^2\Sigma^2}{\eta} \right] E, \tag{31.}$$

where $\mathcal{E} = (\epsilon/2) \int_0^h (\partial_z \phi)^2 dz$ is the electrostatic energy per unit surface introduced in Section 3.3.1. It appears here that slippage has an additive contribution to the EO current, which strikingly does not depend on any electrolyte properties.

We now consider the result in two limiting cases. First, in the thin–Debye layer limit, by comparing with Equation 25, one may identify

$$I_{eo} = \frac{k_B T}{2\pi \ell_B \eta D} I_{ep}^{surf} + 2w \frac{be^2\Sigma^2}{\eta} E, \tag{32.}$$

where I_{ep}^{surf} is the surface contribution to the EP current. To quantify the importance of the EO contribution, one may compute the analogue of a Péclet number:

$$Pe = \frac{I_{eo}}{I_{ep}^{surf}} = \frac{3}{2} \frac{d_i}{\ell_B} \left(1 + \frac{b}{\ell_{GC}} \right). \tag{33.}$$

We have introduced here the ion diameter, d_i, by using the Einstein relation $D = k_B T/(3\pi \eta d_i)$ and we recall that $\ell_{GC} = (2\pi \Sigma \ell_B)^{-1}$. In water at room temperature the ion diameter is $d_i \sim \ell_B \sim 0.7$ nm; therefore, in the absence of slippage, the EO contribution is of the same order as the surface EP contribution, $Pe \sim 1$. For reference, the table in the **Supplemental Appendix** lists values of the Gouy–Chapman length for typical surface charge values. As these are typically in the

Supplemental Material >

nanometer range, even in the case of moderate slippage ($b \sim 10$ nm), there is a strong enhancement of the EO contribution by a factor b/ℓ_{GC}. The threshold confinement below which the resulting surface contribution dominates over the bulk contribution is given by a rescaled Dukhin length: $\ell^*_{Du} = (b/\ell_{GC})\ell_{Du}$.

Second, in the Debye overlap regime, the EO current is readily determined from Equation 29, since the ion densities may then be considered uniform across the channel and are given by Equation 23. Uniform ionic densities also imply that the flow has no longer a surface but rather a volume driving. It is simply a Poiseuille flow, with the pressure gradient $\Delta P/L$ replaced by the electric driving force $e(\rho_+ - \rho_-)E$. Altogether one obtains

$$I_{eo} \simeq \frac{wh}{3\eta} e^2 \Sigma^2 \left(1 + \frac{6b}{h}\right) E. \qquad 34.$$

Since in the Debye layer overlap regime it makes no more sense to distinguish a surface and a bulk contribution, we define the Péclet number as the ratio of the EO current to the total EP current:

$$Pe = \frac{I_{eo}}{I_{ep}} = \frac{d_i}{\ell_B} \frac{h}{4\ell_{GC}} \frac{1 + 6b/h}{\sqrt{1 + (h/\ell_{Du})^2}}. \qquad 35.$$

Figure 5*d* illustrates the dependence of this Péclet number on h and ℓ_{GC}, with $\rho_s = 10^{-2}$ M so that there is overlap of the Debye layers. In the absence of slippage, the EO contribution dominates only for high surface charges. However, if a small slip length, $b = 5$ nm, is introduced, the Péclet number exceeds 1 for all reasonable surface charges. Indeed, the Péclet number is then essentially determined by the ratio b/ℓ_{GC}. This highlights that in the Debye overlap regime, ionic conduction should be mostly driven by electro-osmosis.

If strong EO flows are expected, then the reciprocal effect, streaming current, is expected to be large as well. The streaming current results from the application of a pressure gradient $\Delta P/L$: In the regime of Debye layer overlap, the charge density $2\Sigma/h$ is simply dragged along by the Poiseuille flow. The current reads

$$I_{str} \simeq hw \frac{eh\Sigma}{6\eta} \left(1 + \frac{6b}{h}\right) \frac{\Delta P}{L} \equiv -hw \frac{\epsilon\zeta}{\eta} \frac{\Delta P}{L}, \qquad 36.$$

where we have phenomenologically defined the zeta potential (ζ) via the streaming mobility. Independent measurements of the surface charge through the voltage-driven current and of the zeta potential from the pressure-driven current may allow one in principle to estimate the slip length, b. Such an estimate does not replace a direct measurement, however, in particular because the slip length may directly depend on surface charge (Xie et al. 2020), and additional charge–surface coupling effects may also occur, as we discuss below.

3.3.5. Surface modifications to Poisson–Nernst–Planck theory. A remark is in order at this point concerning the nature of surface charge, which we have so far assumed to be constant, whatever the conditions. Usually, surface charge is considered to result from the acid–base reactivity of the surface when dipped into water, of the type $[AH]_s \rightarrow [A^-]_s + H^+$, where the negative group $[A^-]_s$ remains fixed on the surface, while the proton diffuses in solution. In the case of the air–water interface, surface charge may result from the adsorption of hydronium ions (Mamatkulov et al. 2017), or from charged impurities. The adsorption of surfactant impurities was also proposed as a charging mechanism for general hydrophobic surfaces (Uematsu et al. 2019). Graphite and hBN, which are of particular relevance in nanofluidics, have a priori no obvious acid–base reactivity in water, but they may develop a surface charge, through chemisorption or physisorption of hydroxide ions, as inferred from experiments (Secchi et al. 2016b, Siria et al. 2013) and recently confirmed by ab initio simulations (Grosjean et al. 2019). Such a picture of surface charge implies that it may actually depend on electrolyte concentration, which is an example of charge regulation.

Qualitatively, the salt concentration affects the surface potential and therefore the concentration of H^+ and OH^- ions at the surface, which in turn affects the chemical (or the adsorption) equilibrium that governs the surface charge. Such charge regulation has been invoked to explain several experiments on carbon nanotubes, where a scaling $I \propto \rho_s^{1/2}$ or $I \propto \rho_s^{1/3}$ has been observed (Liu et al. 2010, Pang et al. 2011, Secchi et al. 2016b). Various models have been developed (Biesheuvel & Bazant 2016, Manghi et al. 2018, Uematsu et al. 2018, Secchi et al. 2016b) that predict a rich panorama of different sublinear scalings of conductance with salt concentration, depending on the conditions.

A further step that may be required to accurately describe the surface charge is to take into account its mobility. Surfaces charges may be mobile when embedded in lipid bilayers or, with more relevance to nanofluidics, when resulting from adsorbed ions. For instance, Grosjean et al. (2019) showed in simulations that physisorbed hydroxide ions on graphene surfaces retain a high lateral mobility. The effect of a mobile surface charge on ion and fluid transport coefficients (in the thin Debye layer regime) was the subject of several investigations (Maduar et al. 2015, Mouterde & Bocquet 2018, Silkina et al. 2019). Using the framework of Mouterde & Bocquet (2018), in addition to the water–wall friction coefficient λ, one may introduce two new friction coefficients: λ_-, between the adsorbed (negative) ions and the wall, and ξ_-, between the adsorbed ions and the fluid. The force balance on the interfacial fluid layer results in a modified partial-slip boundary condition involving the tangential electric field at the surface:

$$b_{\rm eff}\partial_z v|_{z=0} = v|_{z=0} - e\frac{\xi_-}{\xi_- + \lambda_-}\frac{b_{\rm eff}}{\eta}\Sigma(-\partial_x\phi)|_{z=0}, \qquad 37.$$

where the effective slip length is

$$b_{\rm eff} = \frac{b}{1 + \frac{\lambda_-\xi_-}{\lambda(\lambda_- + \xi_-)}\Sigma}. \qquad 38.$$

The slip length is therefore reduced by the surface charge mobility, and the boundary condition involves an extra electric term. This has in general a moderating effect on the transport coefficients. For example, in the case of the streaming current, the fluid brings along surfaces charges in addition to the counterions, so that the total current is reduced. Notable exceptions are diffusio-osmotic mobility and conductance: The overall ionic conductance increases when surface charges are able to move in response to the electric field.

We have just introduced ion–wall and ion–water friction for adsorbed ions in the interfacial layer. Now, for the smallest accessible channels, which are comparable to the ion size (Lee et al. 2010, Radha et al. 2016), such friction needs to be taken into account for all the ions and should appear at the level of the transport equations. This was proposed, for instance, to rationalize the nonlinear voltage–pressure couplings observed in angstrom-scale slits by Mouterde et al. (2019). They observed that the streaming mobility μ, defined by $I_{\rm str} = hw\mu\Delta P/L$, depends on the applied voltage in a qualitatively different way for graphite and BN slits. In the proposed surface PNP model, the ion–wall ($\lambda_\pm$) and ion–water ($\xi_\pm$) friction coefficients are introduced in the same way as above, except they no longer apply to adsorbed surface charge ions, but to all the regular salt ions. The equivalents of the Smoluchowski and Stokes equations need then to be rederived by considering the force balance on a single ion and on an element of fluid, respectively, as shown in the **Supplemental Appendix**.

Supplemental Material >

There is a rich phenomenology to be harnessed from the new couplings that appear when all components of the nanofluidic system interact with the surfaces. Nevertheless, such surface PNP theory is still in its infancy, and it requires input from more microscopic modeling in order to estimate the various friction coefficients that have been introduced. It even raises mathematical

difficulties in the writing of a 1D Poisson equation, whose Green's function has infinite range. Finally, the relevance of this phenomenological theory should be assessed in light of the correlation and structuring effects—specific to the smallest scales—that are be described in the next section.

4. BEYOND THE CONTINUUM DESCRIPTION

In this section, we focus on the specific nanoscale effects that are not described in the framework of continuum hydro- and electrodynamics. These effects mainly originate from thermal fluctuations, interparticle correlations, and structuring effects, and, as such, they require theoretical tools that bridge the gap between physics of continuous media and statistical mechanics.

4.1. Fluctuations

As a first step beyond continuum theory, in this section we discuss fluctuations, both of the confining walls and of the fluid itself.

4.1.1. Fluctuating hydrodynamics. The relative particle-number fluctuations in an open system of N particles scale as $1/\sqrt{N}$. In a nanopore of radius 1 nm and length 10 nm, there are on average about 1,000 water molecules, and these fluctuations are of a few percent and already not negligible. Fundamentally, the description of such fluctuations requires a statistical mechanics framework, such as density functional theory (Barrat & Hansen 2003). However, these approaches remain quite formal and difficult to implement, particularly for finite-length pores, which are not translationally invariant systems.

A simpler coarse-grained approach to fluctuations—the so-called fluctuating hydrodynamics (FH)—has been introduced by Landau & Lifshitz (1977). In FH, a random stress tensor $\mathbf{S}$ is added to the Navier–Stokes equation:

$$\rho\partial_t\mathbf{v} + \rho(\mathbf{v}\cdot\nabla)\mathbf{v} = -\nabla p + \eta\Delta\mathbf{v} + \nabla\cdot\mathbf{S}, \qquad 39.$$

where ρ is the mass density of the fluid and $\mathbf{S}$ satisfies a fluctuation-dissipation theorem, $\langle S_{ij}(\mathbf{r},t)S_{kl}(\mathbf{r}',t')\rangle = 2\eta k_\mathrm{B}T(\delta_{ij}\delta_{kl}+\delta_{il}\delta_{jk})\delta(\mathbf{r}-\mathbf{r}')\delta(t-t')$, similarly to the fluctuating force in a Langevin equation. This description introduces thermal fluctuations in a setting where, otherwise, a continuum hydrodynamic description holds. FH has been extensively discussed in the literature (Fox & Uhlenbeck 1970, Hauge & Martin-Lof 1973, Mashiyama & Mori 1978) and we only consider here its basic implications for fluid transport in a nanopore.

In standard hydrodynamics, the fluid inside a nanopore is at rest when subject to no external force. The effect of fluctuations is to induce a stochastic flow through the nanopore, which can be pictured as a stochastic motion of the fluid center of mass (CM). Detcheverry & Bocquet (2012) solved the FH equations for the velocity correlation function and found that the CM motion was described by a non-Markovian Langevin equation of the type

$$m\frac{\mathrm{d}v}{\mathrm{d}t} = -\int_{-\infty}^{t}\mathrm{d}t'\xi(t-t')v(t') + F(t), \qquad 40.$$

where the random force $F(t)$ and the memory kernel ξ are related by $\langle F(t)F(0)\rangle = 2k_\mathrm{B}T\xi(t)$. The memory kernel is indeed nontrivial (i.e., not reduced to a δ function), as confirmed by molecular dynamics (MD) simulations (Detcheverry & Bocquet 2013). Memory effects in the diffusion of fluid inside a nanopore are indeed expected from the analysis of relevant timescales. A nanopore of radius R and length L contains a mass $m = \rho\pi R^2 L$ of fluid, and its friction coefficient on the wall can be calculated from the Navier–Stokes equation as $\xi_\mathrm{s} \approx 8\pi\eta L$. The velocity of the fluid CM

then relaxes on a timescale $\tau \sim m/\xi_s \sim R^2/\nu$. But R^2/ν is the time required for fluid momentum to diffuse across the nanopore, that is, the time for the wall friction force to establish itself. Therefore, the friction force may not adapt instantaneously to the CM velocity, and memory effects are to be expected.

Properties that are determined by short-timescale dynamics may be affected by those memory effects, as was shown to be the case for solute mobility in confinement (Daldrop et al. 2017). More generally, memory effects play an important role in barrier-crossing processes (Kappler et al. 2018). But other properties only depend on the long-timescale dynamics. In particular, the fluid CM diffusion coefficient, given by $\mathcal{D} = k_B T/(2\int_0^\infty \xi(t)\,dt)$, reduces to the Einstein expression $\mathcal{D} = k_B T/\xi_s$, which would be expected if the diffusion was Markovian. Similarly, the hydrodynamic slip length b is found to satisfy a Green–Kubo relation, whatever the form of the memory kernel $\xi(t)$ (Bocquet & Barrat 2013).

From a practical perspective, one may evaluate the diffusion coefficient, $\mathcal{D}$. From the Einstein relation, and the assumption of Poiseuille flow with slip length b, one obtains

$$\mathcal{D} = \frac{k_B T}{\xi} = \frac{k_B T}{\frac{8\pi\eta L}{1+4b/R} + 3\pi^2\eta R}, \qquad 41.$$

where, in the most general case, the friction coefficient ξ has two contributions, one from the channel interior and one from the entrance effects (Detcheverry & Bocquet 2012). Overall, the fluid CM diffusion $\mathcal{D}$ can be seen as a supplementary contribution to the diffusion coefficient of a particle inside the nanopore. If the size of the particle is comparable to that of the nanopore, its self-diffusion is strongly hindered (Renkin 1954) and the fluid contribution may actually dominate the particle diffusion (Detcheverry & Bocquet 2012).

4.1.2. Noise. Thermal fluctuations are at the origin of the noise in ionic current measurements through a nanopore. At zero applied voltage, the total noise amplitude satisfies the Nyquist relation, $\langle I^2\rangle = 2k_B TG$, where G is the nanopore conductance. The EO term in the conductance makes a supplementary contribution to the noise, which can actually be traced back to the hydrodynamic fluctuations of the fluid CM described in the previous section (Detcheverry & Bocquet 2012).

When resolved in frequency, numerous experiments on artificial nanochannels (Hoogerheide et al. 2009, Secchi et al. 2016b, Siwy & Fuliński 2002, Smeets et al. 2008, Tasserit et al. 2010) and biological pores (Bezrukov & Winterhalter 2000, Wohnsland & Benz 1997) have shown that the current spectrum exhibits pink noise, that is, noise that scales with frequency f as $f^{-\alpha}$, with α in the range 0.5–1.5. Such a spectrum is traditionally described by the empirical Hooge's law (Hooge 1969):

$$\langle \delta I^2\rangle(f) = A\frac{\langle I^2\rangle}{f^\alpha}, \qquad 42.$$

with A a coefficient inversely proportional to the number of charge carriers. Notably, in experiments, the $f^{-\alpha}$ scaling is observed down to frequencies below 1 Hz, which shows that some correlations in the system under study exist even at such low frequencies. Correlations between ions have been put forward as a possible origin for the pink noise (Zorkot et al. 2016). However, Gravelle et al. (2019) demonstrated in MD simulations that pink noise persisted even with non-interacting ions, if reversible ion adsorption was allowed on the channel wall. For simple diffusive dynamics, the longest correlation time that may be expected for adsorption–desorption processes is R^2/D, with R the pore radius and D the ion diffusion coefficient. For a 10-nm pore, this would correspond to a frequency cutoff of 100 MHz, below which the noise spectrum should be flat. Such

a high cutoff frequency is in clear contradiction with experiment. However, Gravelle et al. showed that in the presence of reservoirs, excursions of ions outside the pore coupled to adsorption–desorption processes on the pore surface result in ionic correlations on much longer timescales, hence predicting pink noise down to very low frequencies.

4.1.3. Wall fluctuations. So far, we have only considered thermal fluctuations of the fluid itself. However, the confining walls might also be subject to fluctuations. Wall fluctuations are known to enhance fluid self-diffusion by inducing flows, through the Taylor–Aris mechanism (Aris 1956, Taylor 1953). In contrast, static constrictions slow down diffusion in a channel through Fick–Jacobs entropic trapping (Malgaretti et al. 2014, Reguera & Rubí 2001).

A very general framework for evaluating the self-diffusion coefficient for a fluid confined in a fluctuating channel was developed by Marbach et al. (2018). In a slit-like channel of height h, the fluctuation-corrected diffusion coefficient D is formally related to the spectrum of wall fluctuation $S(k, \omega)$ by

$$D = D_0 \left[1 - \frac{1}{h^2} \int \frac{\mathrm{d}k\mathrm{d}\omega}{(2\pi)^2} \frac{(D_0 k^2)^2 - 3\omega^2}{(D_0 k^2)^2 + \omega^2} S(k, \omega) \right], \qquad 43.$$

where D_0 is the bare diffusion coefficient. Equation 43 has two limiting regimes that are governed by a fluctuation-related Péclet number, which may be defined as $Pe = \ell^2/(D_0\tau)$, where ℓ and τ are the characteristic length and timescales of the fluctuations, respectively. The diffusion coefficient is enhanced for $Pe > 1$ ($D = D_0(1 + 3\langle \delta h^2 \rangle / h^2)$) and reduced for $Pe < 1$ ($D = D_0(1 - \langle \delta h^2 \rangle / h^2)$), and both tendencies are observed experimentally (Marbach et al. 2018). Equation 43 thus bridges the limiting Taylor–Aris and Fick–Jacobs results.

The permeability of a fluctuating channel is also expected to be impacted by wall fluctuations. Recently, MD simulations have shown diffusion enhancement due to the propagation of phonons in carbon nanotubes (Cruz-Chú et al. 2017, Ma et al. 2015). However, permeability is related to the diffusion of the fluid CM (see Equation 41), which is different from the fluid self-diffusion, and extending the above framework to CM diffusion remains to be done.

4.2. Fluid Structuring

Moving now to molecular-scale confinement, in this section we discuss the effect of fluid molecular structure on its various properties.

4.2.1. Phenomenology. While a fluid appears disordered at hydrodynamic length scales, its molecular nature manifests itself under confinement in the form of structuring effects. Even at a nonconfined solid–liquid interface, the attractive interactions between the solid and the liquid result in molecular layering, as verified experimentally by X-ray spectroscopy (Cheng et al. 2001). Between two surfaces, a liquid adopts a layered structure even in the absence of interactions simply due to geometrical constraints (Israelachvili & Pashley 1983). The onset of structuring clearly represents the transition from continuum to subcontinuum transport.

The threshold confinement at which this transition occurs has been studied for both planar and cylindrical geometries using MD simulations. For water in carbon nanotubes, Thomas & McGaughey (2009) have found that it retains a bulk-like disordered structure down to a tube diameter of 1.39 nm [(10,10) tube; see the sidebar titled Chiral Indices for an explanation of this notation]. In a (9,9) tube (1.25 nm), water was found to structure in stacked hexagons (see **Figure 6**) and in a single-file chain in a 0.83-nm (6,6) tube. For water between two graphene sheets, four distinct layers could be observed when the distance between the sheets was 1.35 nm

CHIRAL INDICES

The pair of integers (n, m) may be used to uniquely specify the geometry of a carbon nanotube, that is, how a given tube may be obtained by rolling up a graphene sheet. Let $\mathbf{a}_1$ and $\mathbf{a}_2$ be the unit vectors of the graphene honeycomb lattice. Then, the vector $\mathbf{C} = n\mathbf{a}_1 + m\mathbf{a}_2$ joins any two atoms that fall onto each other when the graphene sheet is rolled into an (n, m) tube.

(Neek-Amal et al. 2016), and a single monolayer of water was observed for confinement below 0.8 nm (Neek-Amal et al. 2018). It should further be noted that an exotic square ice phase for monolayer water between two graphene sheets has been reported (Algara-Siller et al. 2015).

In the subcontinuum regime, transport properties show strong qualitative deviations from bulk expectations. The MD simulations of Thomas & McGaughey (2009) showed nonmonotonic permeability for carbon nanotubes as a function of diameter, and similar observations were made for the capillary filling velocity of carbon nanotubes, studied by Gravelle et al. (2016). On the experimental side, this behavior can be put in perspective with recent results by Radha et al. (2016) for capillary-driven flow through slit-like graphene channels, where a peak in flow rate around 1.3-nm confinement was observed.

4.2.2. Disjoining pressure. Thermodynamically, the effect of molecular fluid structuring may be described by a supplementary contribution to the pressure, the so-called disjoining pressure, which, for a fluid confined between two walls of area $\mathcal{A}$ separated by a distance h, in equilibrium with a reservoir at pressure P_0, is defined in full generality as

$$\Pi_d(h) = -\frac{1}{\mathcal{A}}\left(\frac{\partial G}{\partial h}\right), \qquad 44.$$

where G is the Gibbs free energy of the whole system (Barrat & Hansen 2003, Israelachvili 2011).

In principle, G varies with h because of distance-dependent interactions between the surfaces; the disjoining pressure can then be seen as the force the fluid needs to exert in order to oppose

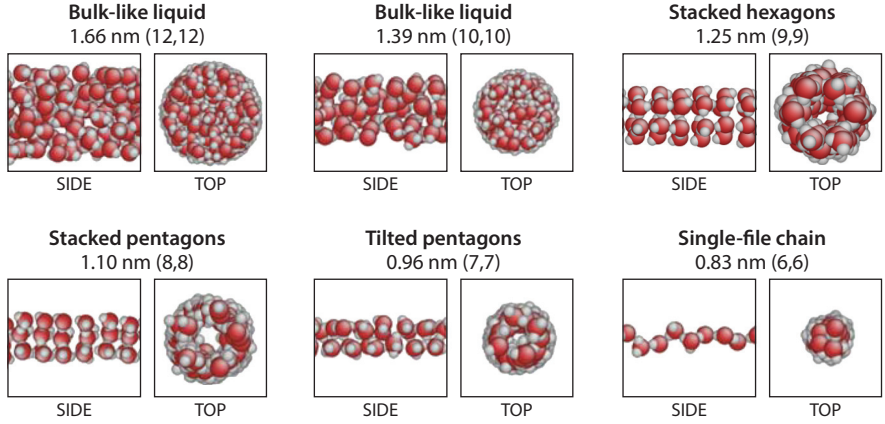

Figure 6

Molecular dynamics simulation snapshots of water structure inside carbon nanotubes of different radii. Figure adapted with permission from Thomas & McGaughey (2009), copyright 2009 American Physical Society.

those interactions. These are generally of two types. On the one hand, there are van der Waals interactions that scale algebraically as h^{-2}, yielding a contribution $\Pi_{\mathrm{vdW}} = -\frac{A_{\mathrm{H}}}{6\pi h^3}$ to the disjoining pressure, with A_{H} the Hamaker constant (although more complex dependencies may occur in specific geometries). On the other hand, electrostatic interactions lead to contributions that scale exponentially with the distance h due to ionic screening. The combination of these two interaction terms is the basis for the DLVO (Derjaguin–Landau–Verwey–Overbeek) theory.

Now, if there is fluid structuring that depends on confinement, it makes a supplementary contribution to the variation of G. This contribution exists even for a hard sphere fluid due to excluded volume effects and is purely entropic in nature. It quantifies essentially how much the structure of the fluid in confinement differs from the one in the bulk. For hard spheres of diameter σ, the disjoining pressure is usually described by the expression (Israelachvili 2011, Kralchevsky & Denkov 1995)

$$\Pi_{\mathrm{d}}(h) = -\rho_\infty k_{\mathrm{B}} T \cos(2\pi h/\sigma) e^{-h/\sigma}, \qquad 45.$$

where ρ_∞ is the bulk density. This is an oscillating function of h that decays to 0 at large h, where there is no more fluid structuring. It is bounded by $\Pi_{\mathrm{d}}(0) = \rho_\infty k_{\mathrm{B}} T$, which evaluates to about 1,000 bar for liquid water at room temperature. In practice, for fluid flow measurements where a pressure drop is imposed between two reservoirs, this (huge) contribution to the pressure does not intervene directly. However, in a capillary flow geometry, which involves liquid–vapor interfaces, the disjoining pressure may be much larger than the bare capillary pressure and act as the main driving force. Indeed, the capillary pressure drop across a meniscus of radius $R = 1$ nm is typically $2\gamma/R = 140$ bar (for water with surface tension, $\gamma = 72$ mN/m). Driving by disjoining pressure was observed in simulations of carbon nanotube capillary filling (Gravelle et al. 2016), where the subtle dependence of the water molecular structure—and therefore of the disjoining pressure—on nanotube radius resulted in the imbibition velocity displaying oscillatory behavior versus the confinement. Experimentally, a similar phenomenology was observed by Radha et al. (2016), who measured the capillary flow of water across angstrom-scale slits and found a nonmonotonous dependence of the evaporation rate on confinement. These measurements could be interpreted in terms of disjoining pressure, which was indeed found to be on the order of 1,000 bar in MD simulations of the experimental system (Neek-Amal et al. 2018).

4.2.3. Descriptions of fluid transport. A first understanding of subcontinuum transport may be provided by extending the continuum description with effective, confinement-dependent values for density, viscosity, and slip length. In a layered fluid, the density in each layer is generally higher than in the bulk, and a general trend is that viscosity increases (Schlaich et al. 2017). More exotically, an oscillating viscosity as a function of confinement was observed in simulations of water between two graphite slabs (Neek-Amal et al. 2016). Neek-Amal et al. (2018) were able to reproduce the experimental results of Radha et al. (2016) by using simulated values of disjoining pressure, along with a Poiseuille formula with effective density and viscosity; however, they assumed a viscosity-independent slip length. Now, in general, care should be taken in defining a viscosity for a structured fluid: As its density is nonuniform, a position-dependent viscosity should be introduced in order to describe the details of the flow profile. For confinement below five molecular diameters (in the case of a Lennard–Jones fluid), Travis et al. (1997) have shown that even a position-dependent viscosity is not sufficient and a nonlocal viscosity kernel should be used (Zhang et al. 2004). Ultimately, for confinement below a few molecular layers (typically 1 nm for water), the notion of viscosity itself—which is intrinsically a continuum quantity—loses its fundamental meaning.

Nevertheless, a simple picture of subcontinuum fluid transport is possible in the case of large slippage, since surface friction then becomes the main mechanism resisting fluid transport. Indeed, this appears when looking at the limit $b \gg R$ in the Poiseuille formula of Equation 7, which yields

$$v = \frac{Rb}{2\eta L}\Delta P = \frac{R}{2\lambda L}\Delta P \qquad 46.$$

for the average flow velocity, where we have obtained the second equality by relating the slip length to the liquid–wall friction coefficient, λ, as $b = \eta/\lambda$; note that, for simplicity, we disregard entrance effects. The viscosity does not enter the permeability, as expected for surface-dominated friction. The fluid moves indeed in the channel as a single block, and dissipation only intervenes at the surface. The crucial parameter governing the transport is then the solid–liquid friction coefficient, λ. A model for evaluating λ, tested against MD simulations of water in carbon nanotubes, was proposed by Falk et al. (2010). They obtained

$$\lambda \approx \frac{\tau}{k_B T} f_{\mathbf{q}_0}^2 S(\mathbf{q}_0), \qquad 47.$$

where $\mathbf{q}_0$ is the wave vector corresponding to the solid lattice spacing, $f_{\mathbf{q}_0}$ is the Fourier component of the fluid–solid interaction potential at that wave vector, $S(q)$ is the liquid structure factor, and τ is the correlation time of the force between the solid and the liquid, which is found not to depend on confinement. In this way, λ is directly related to the liquid structure and to the liquid–wall interaction. Such a friction-dominated approach was applied successfully, for example, to predict the permeability of ultraconfined alcanes in a nanoporous matrix, showing a scaling dependence of the permeance on the alcane length (Falk et al. 2015). However, predicting the solid–liquid friction coefficient remains mostly an open problem. As we discuss below (see Section 4.2.6), its determination in MD simulations still remains ambiguous quantitatively, and the role of underlying quantum effects should be assessed.

4.2.4. Ultimate structuring: single-file transport. The most extreme type of structuring is single-file arrangement of fluid molecules. In the case of water transport, this is the realm of biological channels (Horner & Pohl 2018b), where water is conducted through subnanometric openings in transmembrane proteins. Single-file transport may also occur in artificial channels: It was observed in MD simulations for carbon (Hummer et al. 2001) and boron nitride (Won & Aluru 2007) nanotubes of 0.8 nm in diameter and more recently was experimentally observed in carbon nanotubes (Tunuguntla et al. 2017). Single-file transport is a field of its own and there are dedicated reviews on the subject (Horner & Pohl 2018b, Köfinger et al. 2011); here we only sketch the main ideas.

The notion of single-file transport and the underlying exclusion transport models are not restricted to the study of confined fluids. Indeed, a general feature of particles in one dimension that cannot cross each other is subdiffusive behavior: The mean-squared displacement of a particle scales with time as $\langle \Delta x^2 \rangle \propto t^{1/2}$, as opposed to linear scaling for normal diffusion (Levitt 1973). Such anomalous diffusion is encountered in a variety of fields (Fouad & Gawlinski 2017) and may be understood in terms of the normal diffusion of vacancies in the 1D chain; in the case of fluid transport, it was studied by Chou (1998, 1999). However, this effect is not expected to play a decisive role in single-file transport through short channels, where vacancies are unlikely to occur (Kalra et al. 2003).

In the case where no vacancies are expected, a simple model was proposed decades ago by Finkelstein (1987) for describing single-file water transport in biological channels. It stems from a global force balance on the water chain and as such is equivalent to Equation 46, which we have derived as a strongly confined limit of the Poiseuille formula. In Finkelstein's model, the chain of

N water molecules (of total length L) moving at velocity v is subject to a friction force, $-N\xi v$, and to a pressure driving, $Nv_w\Delta P/L$, where v_w is the volume of one water molecule. The force balance then leads to

$$v = \frac{v_w}{\xi L}\Delta P, \tag{48.}$$

which is indeed Equation 46, given the identification $\xi = (2v_w/R)\lambda$. In the biophysics literature, the preferred quantity for characterizing a channel's transport properties is the unitary channel permeability, p_f, which is the number of water molecules that crosses the channel per unit time, per unit osmolyte concentration difference applied across the channel, and is therefore expressed in meters cubed per second. For an osmolyte concentration difference $\Delta\rho_s$, the osmotic pressure difference is $k_BT\Delta\rho_s$, and hence the unitary permeability is

$$p_f = \frac{N}{L}\frac{v}{\Delta\rho_s} = \frac{v_w}{aL}\frac{k_BT}{\xi}, \tag{49.}$$

where we have defined $a = L/N$ as the average spacing between water molecules. The diffusion coefficient of the water chain CM may be expressed through the Einstein relation as $D = k_BT/(N\xi)$, and therefore we have $p_f = v_wD/a^2$; hence, the diffusion coefficient and the unitary permeability may be used interchangeably. A typical value for the permeability in biological channels, such as aquaporin or gramicidin A, is in the range of 10^{-14}–10^{-13} cm^3/s, which corresponds to 1–10 water molecules crossing the channel per nanosecond under a 1-bar pressure drop.

In an alternative phenomenological description, transport through the channel is viewed as an activated process with activation energy $\Delta G^\ddagger$ (Horner & Pohl 2018b). The permeability is then expressed in the framework of transition state theory as $p_f = v_w\nu_0 \exp[-\Delta G^\ddagger/k_BT]$, with $\nu_0 \sim 10^{13}$ s^{-1} a molecular attempt frequency. For biological channels, this relation is well verified by independent measurements of p_f and $\Delta G^\ddagger$, with $\Delta G^\ddagger$ on the order of 5 kcal/mol. However, values of $\Delta G^\ddagger$ remains debated for transport measurements in carbon nanotubes (Horner & Pohl 2018a, Tunuguntla et al. 2018).

Although it provides a general guiding line, Finkelstein's formula is challenged in both artificial and biological channels. In the case of protein channels, the assumption of uniformly smooth walls breaks down, since there are discrete hydrogen bonding sites (Horner & Pohl 2018b). Hence p_f is not found to be inversely proportional to channel length (Saparov et al. 2006); rather, it has an exponential dependence on the number of hydrogen bonding sites (Horner et al. 2015). Such an exponential dependence suggests a collective transport mechanism of the water chain, with bursts requiring the breaking of multiple hydrogen bonds at once. There is, however, a notable disagreement between experiments and simulations, as the simulations of water transport through polyalanine channels showed no dependence of p_f on the channel length (Portella et al. 2007).

In simulations of carbon nanotube channels, all single-file water molecules were clearly shown to move in a correlated fashion, thus challenging any description based on a solid–liquid friction coefficient (Hummer et al. 2001): Water transport occurs when all the molecules simultaneously shift by one molecular diameter. These dynamics were successfully described by a continuous-time random-walk model (Berezhkovskii & Hummer 2002) or, equivalently, by diffusion of a collective coordinate of the water molecules (Zhu et al. 2004), which actually echoes our discussion of fluctuations in a more general setting [Equation 40 and Detcheverry & Bocquet (2012)]. Overall, there is still much to understand about the collective motions and subtle surface interactions involved in single-file transport, and it is an active field of research.

4.2.5. Structuring and electrostatics: dielectric anomalies. As confined water becomes structured, its response properties to an external electric field are accordingly modified. When

an electric field **E** is imposed in water, the individual molecules reorient and polarize, creating an electric field themselves. The total electric field **E** is then the sum of the polarization field of the water molecules and of the externally applied field $\mathbf{D}/\epsilon_0$, where **D** is called the electric displacement and ϵ_0 is the vacuum permittivity. In bulk water, the dielectric response, that is, the relation between **D** and **E**, may be expressed through a single scalar quantity, the relative permittivity $\epsilon \approx 80$: $\mathbf{D} = \epsilon\epsilon_0\mathbf{E}$. However, the most general (static) linear response may be anisotropic, space dependent, and nonlocal:

$$D_\alpha(\mathbf{r}) = \epsilon_0 \sum_\beta \int d\mathbf{r}' \epsilon_{\alpha\beta}(\mathbf{r}, \mathbf{r}') E_\beta(\mathbf{r}'). \quad 50.$$

The relative permittivity is then a tensor with components $\epsilon_{\alpha\beta}(\mathbf{r}, \mathbf{r}')$ ($\alpha, \beta \in \{x, y, z\}$). While MD simulations show that the dielectric response in water may be considered local, $\epsilon_{\alpha\beta}(\mathbf{r}, \mathbf{r}') = \epsilon_{\alpha\beta}(\mathbf{r})\delta(\mathbf{r} - \mathbf{r}')$, it becomes anisotropic and space dependent in the vicinity of interfaces as a consequence of the water layering (Bonthuis et al. 2011, 2012). Qualitatively, the orientations of the water dipoles are anticorrelated in the direction perpendicular to the interface, resulting in a reduced permittivity in that direction, while the permittivity is largely unaffected parallel to the interface. In planar confinement, this behavior could be captured by an effective medium model, in which the water is described by a space-independent, but anisotropic, permittivity ($\epsilon_\parallel, \epsilon_\perp$) (the parallel direction is not confined). While $\epsilon_\parallel$ essentially retains its bulk value, $\epsilon_\perp$ is reduced by up to an order of magnitude for confinements below 1 nm (Schlaich et al. 2016, Zhang et al. 2013). Such a reduction of the perpendicular dielectric response was recently observed experimentally for water confined between a graphite and a boron nitride crystal (Fumagalli et al. 2018). A deviation from the bulk value was measured up to nearly 100-nm confinement (**Figure 7**). The results were well described by assuming each interface carried a 7-Å-thick layer of very low permittivity ($\epsilon = 2.1$; "electrically dead water").

An effective medium model based on MD simulations was developed by Loche et al. (2019) for cylindrical confinement of water in carbon nanotubes. Similarly to the planar case, the radial permittivity was found to be reduced by up to an order of magnitude for tube radii smaller

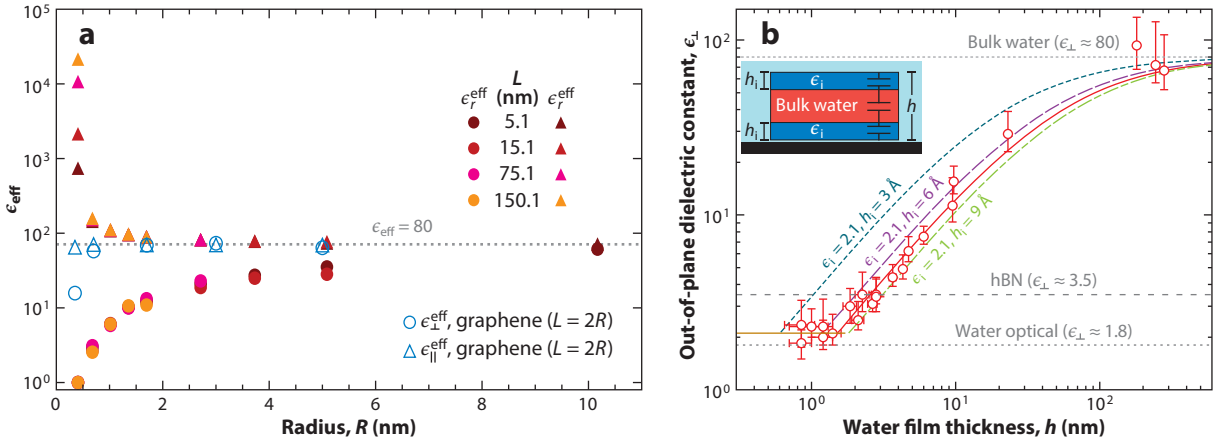

Figure 7

Dielectric anomalies due to fluid structuring. (*a*) Components ($\epsilon_r^{eff}, \epsilon_z^{eff}$) of the dielectric permittivity tensor of water in a carbon nanotube, as a function of nanotube radius, as determined from molecular dynamics simulations by Loche et al. (2019). (*b*) Experimental results for the transverse dielectric constant of water in planar confinement as a function of confinement width. Panel adapted with permission from Fumagalli et al. (2018), copyright 2018 AAAS.

than 3 nm (**Figure 7**). However, for the smallest tubes (below 1 nm in radius), the longitudinal permittivity was found to increase with respect to its bulk value, and it skyrocketed 1 to 3 orders of magnitude in a 0.4-nm-radius tube, where water is in a single-file arrangement. Knowledge of these modified dielectric properties is important when considering ion transport in strong confinement, as discussed below (see Section 4.3.1).

4.2.6. Limits of molecular dynamics. We close this section on liquid structuring with a word of warning. Many of the results we have presented so far have been obtained using classical MD simulations, and like any type of simulation, these come with some underlying assumptions. In particular, as we are dealing with strongly confined fluids where all the molecules interact with the confining surface, the modeling of that surface plays an increasingly important role. Since the solid is represented by rigid spheres interacting with classical force fields, no electron dynamics may be described by the simulation. However, some coupling between water and electron dynamics may be expected, based on a length-scale argument. The maximum of the dielectric response of a solid indeed occurs at a length scale k_{TF}^{-1}, where k_{TF} is the Thomas–Fermi wave vector (Mahan 2000). Typically, $k_{\mathrm{TF}}^{-1} \approx 1$ nm in graphite; hence the electrons in graphite could be expected to respond to the dynamics of individual water molecules.

There is growing evidence that such electron–water couplings indeed occur. A first consequence of taking into account electron dynamics is that a solid should appear polarizable: In simulations, the fluctuations of water next to a graphite surface were found to be strongly affected by the polarizability of carbon atoms (Misra & Blankschtein 2017). Experimentalists have observed the induction of an electronic current by a water flow inside a carbon nanotube, as well as the reverse phenomenon (Ghosh et al. 2003, Rabinowitz et al. 2020).

These results call for caution in the interpretation of MD simulations, which, as we have pointed out, lack electron dynamics. They also call for the development of new simulation methods that would take such dynamics into account, while not being limited by the very small system size of ab initio simulations.

4.3. Electrostatics in Extreme Confinement

In this section, we discuss a few aspects of the behavior of ions below the continuum limit. We describe how the confinement modifies ionic interactions, as well as possible consequences for ion transport.

4.3.1. Ionic interactions and self-energy. In bulk water, ions interact via a Coulomb potential, $\phi(r) = e/(4\pi\epsilon_0\epsilon_{\mathrm{w}}r)$, where ϵ_{w} is the relative water dielectric permittivity. But inside a nanochannel, ions are no longer surrounded by a homogeneous fluid, and their interaction potential may be affected by the dielectric properties of the confining medium. In order to assess the importance of this effect, we consider the simple situation where an infinitely long cylindrical channel of radius R is filled with water with isotropic permittivity ϵ_{w}, and where the medium outside the channel is a homogeneous dielectric of permittivity ϵ_{s} (typically, $\epsilon_{\mathrm{s}} \ll \epsilon_{\mathrm{w}}$). The electrostatic potential around an ion placed in the middle of the channel can then be determined by solving Poisson's equation in the presence of the dielectric discontinuities, which has been done analytically by several authors (Kavokine et al. 2019, Levin 2006, Parsegian 1969, Teber 2005).

The complicated analytical result may be interpreted in the following way (see **Figure 8**). At short distances (much smaller than the channel radius), only the dielectric response of the water is visible and the potential is $\phi(x) \sim 1/(\epsilon_{\mathrm{w}}x)$. At long distances (much larger than the channel radius),

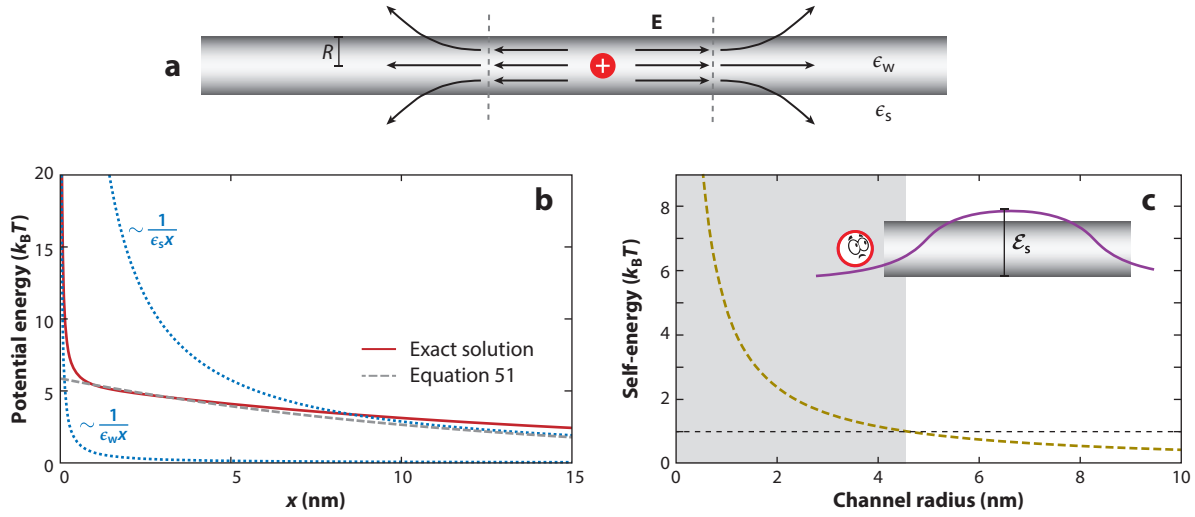

Figure 8

(*a*) Schematic representation of the electric field lines around an ion confined in a narrow channel, with dielectric permittivity ϵ_w inside and ϵ_s outside. (*b*) Potential generated along the axis by an ion confined in a channel of radius 2 nm. (*c*) Born self-energy $\mathcal{E}_s$ of a monovalent ion inside an infinite cylindrical channel, as a function of channel radius R, computed following Teber (2005). (*Inset*) Schematic of the self-energy barrier faced by an ion upon entering a narrow channel.

it is the dielectric response of the confining medium that matters and we have $\phi(x) \sim 1/(\epsilon_s x)$. At intermediate distances, the electric field lines are essentially parallel to the channel due to the dielectric contrast, $\epsilon_w \gg \epsilon_s$, and the potential, which is well described by an exponential function, resembles a 1D Coulomb potential:

$$\phi(x) \approx \frac{e\alpha}{2\pi\epsilon_0\epsilon_w R} e^{-x/(\alpha R)}, \qquad 51.$$

with α a numerical coefficient that depends on the ratio ϵ_w/ϵ_s ($\alpha = 6.3$ for $\epsilon_w/\epsilon_s = 40$) (Teber 2005). It is notable that so far no assumption on the channel radius has been made, so that formally this 1D regime exists for a channel of any size. However, it is only relevant if it leads to ion–ion interactions stronger than k_BT, that is, for $e\phi(R) > k_BT$ in the case of a monovalent ion. This defines a limiting channel radius, below which ionic interactions are affected by the confining medium: $R_c \sim 7.5$ nm. These modified Coulomb interactions therefore may have some effect in any single-digit nanopore, and they have essentially two practical consequences.

First, because ions produce a stronger Coulomb potential in confinement than in the bulk, they have a larger Born self-energy. This phenomenon was pointed out decades ago by Parsegian (1969) in the case of ions crossing lipid bilayers and has since then been commonly considered in the study of biological ion channels. For small channels where the 1D contribution to the potential dominates, the additional self-energy due to confinement is $\mathcal{E}_s = e\phi(0)/2$, with $\phi(x)$ given by Equation 51. An expression valid for any R was obtained by Teber (2005), and it is plotted in **Figure 8**. It shows that $\mathcal{E}_s$, which represents a supplementary energy barrier for entering the channel, is larger than k_BT up to $R \sim 4$ nm. To illustrate the consequence of this Born self-energy, let us consider a neutral channel in the absence of correlation effects: A barrier $\mathcal{E}_s = 4k_BT$ reduces the ionic concentration by a factor $e^{\mathcal{E}_s/(k_BT)} = 100$.

Second, increased Coulomb interactions with respect to the bulk may actually result in correlation effects. To assess the potential importance of correlations, one may introduce a coupling parameter, $\Gamma = e\phi[(\pi R^2\rho)^{-1}]/(k_BT)$, where ρ is the ion concentration inside the channel, so that

$(\pi R^2 \rho)^{-1}$ is the average distance between ions (Bocquet & Charlaix 2010). Let us take as an example a channel of radius 2 nm, where we have $\mathcal{E}_s \sim 2.5 k_B T$ from Equation 51. An effective Coulomb potential of magnitude $\sim 5 k_B T$ then extends around an ion over a distance $\alpha R \sim 10$ nm. Therefore, for concentrations above $\rho = 10^{-2}$ M, Γ is greater than 1 and correlations are expected to become important.

Several remarks can be made here. A first point is that we have considered monovalent ions so far; for ions of valence z, the self-energy, for example, would be multiplied by a factor z^2. Second, we have been assuming for simplicity that water has an isotropic permittivity ϵ_w. We have highlighted in the previous section that this assumption breaks down in cylindrical channels of radius smaller than 5 nm, and, although it does not affect the qualitative phenomenology, dielectric anisotropy, as predicted by Loche et al. (2019), should then be taken into account. It mainly affects the behavior of the potential at short distances $x \leq R$. Third, we should mention that when entering a channel smaller than its hydrated radius, an ion pays an additional energy penalty due to the shedding of its hydration shell (Epsztein et al. 2019, Richards et al. 2012). For chloride, the total hydration energy is as high as 155 $k_B T$, but the hydrated radius is 0.4 nm, so that only partial dehydration arises and only for the smallest pores. Finally, we have assumed that the confining medium is a dielectric medium with uniform permittivity. This is a good model for a lipid membrane, but artificial confining materials may have a variety of electronic properties (see Section 4.2.6), and their influence on effective Coulomb interactions has not been thoroughly investigated. In the case of confinement by a perfect metal, the ionic interactions were found to be exponentially screened over a distance on order of the channel radius (Kondrat & Kornyshev 2011, Loche et al. 2019). Such effective interactions were found to lead to like-charge attraction in ionic liquids confined in carbon nanopores (Futamura et al. 2017).

4.3.2. Ion transport beyond the mean field. We have highlighted in the previous paragraph that correlations may become important in ion transport through single-digit nanopores. If this is the case, then mean-field theories, such as the PNP framework, may not be directly applied, and determination of equilibrium properties, such as ion concentrations inside the nanopore, requires some form of exact statistical mechanics. In systems with high aspect ratio (typically nanotubes), the problem can be reduced to a 1D model of the Ising or 1D Coulomb gas type, and the partition function may then be exactly computed through a (functional) transfer matrix formalism (Kavokine et al. 2019, A.A. Lee et al. 2014, Zhang et al. 2006). Outside of the 1D geometry, variational field theory methods may be used (Buyukdagli et al. 2010), and methods for incorporating ion pairs into Poisson–Boltzmann theory have been developed (Levin 2002). A general feature of these calculations (Buyukdagli et al. 2010, Zhang et al. 2006) is that they predict filling transitions: namely, a nonanalytic behavior of ion concentrations in the nanopore as a function of the salt concentration in the reservoir, which strongly deviates from the mean-field Donnan equilibrium result and may break local electroneutrality (Zhang et al. 2006). One should note, however, that breakdown of electroneutrality does not require ionic correlations and has recently been shown to arise in a mean-field setting (Levy et al. 2020).

If linear response theory applies, then transport properties such as ionic conductance may be determined directly from the concentrations of charge carriers at equilibrium. However, this is no longer the case when correlations are very strong, leading to the formation of tightly bound Bjerrum pairs of oppositely charged ions. This was first realized by Onsager, who showed that in a 3D weak electrolyte—an electrolyte that forms Bjerrum pairs—there is a quadratic current–voltage relation, a phenomenon known as the second Wien effect (Kaiser et al. 2013, Onsager 1934). Bjerrum pairing in 1D confinement was studied by Kavokine et al. (2019), and stable ion pairs were shown to arise typically for confinement below 2 nm, similarly to what was observed

in MD simulations (Nicholson & Quirke 2003). The pairing resulted in some very nonlinear behavior governed by discrete particle effects, echoing the phenomenology of Coulomb blockade (Beenakker 1991, Kaufman et al. 2015). As such, ion correlations produced quantized transport behavior in a purely classical system.

The coupling of ion transport to fluid transport in the non-mean-field, nonlinear regime remains largely unexplored, although it promises a rich phenomenology. As an example, a recent simulation (Li et al. 2017) found that pressure-driven water flow through a nanochannel could be blocked by an ion tightly bound inside. Lastly, we should mention, at the frontier of subcontinuum ion transport, the Grotthuss-like translocation of protons, which has been observed in a single file (Tunuguntla et al. 2017) and a single plane (Gopinadhan et al. 2019) of water but remains poorly understood in strongly confined systems.

5. CONCLUSION

This review has explored some defining aspects of fluid transport at the nanoscale. We started from continuum theory and reduced the scale down to its limit of applicability; we then explored phenomena that occur below the continuum limit and gave indications of appropriate theoretical descriptions to tackle them. The main points summarized below were made. Overall, fluids in molecular-scale confinement are largely an uncharted territory for theory, and recent experiments call for the development of theoretical tools beyond those described in this review.

SUMMARY POINTS

1. Experimental systems for studying fluid transport in molecular-scale confinement are today within reach.
2. Above 10-nm confinement, fluid transport is governed by continuum hydrodynamic equations, with coupling to ion transport and surface effects.
3. Below 10 nm—the domain of so-called single-digit nanopores—thermal fluctuations and electrostatic correlations are increasingly important, challenging continuum and mean-field theory.
4. In few-nanometer confinement, fluid structuring effects and correlations play an overwhelming role.

DISCLOSURE STATEMENT

The authors are not aware of any biases that might be perceived as affecting the objectivity of this review.

ACKNOWLEDGMENTS

L.B. acknowledges funding from the European Union Horizon 2020 framework programme/ERC (European Research Council) advanced grant agreement number 785911-Shadoks. L.B. and R.R.N. acknowledge support from ANR (Agence nationale de la recherche)-DFG (Deutsche Forschungsgemeinschaft) project Neptune. R.R.N. acknowledges funding from the DFG via research platform SFB1114, project number 235221301, project C02, and grant NE810/11. N.K. thanks A. Marcotte for discussions.

LITERATURE CITED

Algara-Siller G, Lehtinen O, Wang FC, Nair RR, Kaiser U, et al. 2015. Square ice in graphene nanocapillaries. *Nature* 519:443–45

Andelman D. 1995. Electrostatic properties of membranes: the Poisson-Boltzmann theory. In *Handbook of Biological Physics*, Vol. 1, ed. R Lipowsky, E Sackmann, pp. 603–42. Amsterdam: Elsevier

Aris R. 1956. On the dispersion of a solute in a fluid flowing through a tube. *Proc. R. Soc. A* 235:67–77

Barrat JL, Hansen JP. 2003. Chapter 7: the density functional approach. In *Basic Concepts for Simple and Complex Liquids*, pp. 179–212. Cambridge, UK: Cambridge Univ. Press

Beenakker CW. 1991. Theory of Coulomb-blockade oscillations in the conductance of a quantum dot. *Phys. Rev. B* 44:1646–56

Berezhkovskii A, Hummer G. 2002. Single-file transport of water molecules through a carbon nanotube. *Phys. Rev. Lett.* 89:064503

Bezrukov SM, Winterhalter M. 2000. Examining noise sources at the single-molecule level: $1/f$ noise of an open maltoporin channel. *Phys. Rev. Lett.* 85:202–5

Biesheuvel PM, Bazant MZ. 2016. Analysis of ionic conductance of carbon nanotubes. *Phys. Rev. E* 94:78–81

Bocquet L. 2014. Nanofluidics: bubbles as osmotic membranes. *Nat. Nanotechnol.* 9:249–51

Bocquet L. 2020. Nanofluidics coming of age. *Nat. Mater.* 19:254–56

Bocquet L, Barrat JL. 2007. Flow boundary conditions from nano- to micro-scales. *Soft Matter* 3(6):685–93

Bocquet L, Barrat JL. 2013. On the Green-Kubo relationship for the liquid-solid friction coefficient. *J. Chem. Phys.* 139:044704

Bocquet L, Charlaix E. 2010. Nanofluidics, from bulk to interfaces. *Chem. Soc. Rev.* 39:1073–95

Bonthuis DJ, Gekle S, Netz RR. 2011. Dielectric profile of interfacial water and its effect on double-layer capacitance. *Phys. Rev. Lett.* 107:166102

Bonthuis DJ, Gekle S, Netz RR. 2012. Profile of the static permittivity tensor of water at interfaces: consequences for capacitance, hydration interaction and ion adsorption. *Langmuir* 28:7679–94

Buyukdagli S, Manghi M, Palmeri J. 2010. Ionic capillary evaporation in weakly charged nanopores. *Phys. Rev. Lett.* 105:158103

Celebi K, Buchheim J, Wyss RM, Droudian A, Gasser P, et al. 2014. Ultimate permeation across atomically thin porous graphene. *Science* 344:289–92

Cheng L, Fenter P, Nagy KL, Schlegel ML, Sturchio NC. 2001. Molecular-scale density oscillations in water adjacent to a mica surface. *Phys. Rev. Lett.* 87:156103

Chmiola J, Yushin G, Gogotsi Y, Portet C, Simon P, Taberna PL. 2006. Anomalous increase in carbon at pore sizes less than 1 nanometer. *Science* 313:1760–63

Choi W, Ulissi ZW, Shimizu SF, Bellisario DO, Ellison MD, Strano MS. 2013. Diameter-dependent ion transport through the interior of isolated single-walled carbon nanotubes. *Nat. Commun.* 4:2397

Chou T. 1998. How fast do fluids squeeze through microscopic single-file pores? *Phys. Rev. Lett.* 80:85–88

Chou T. 1999. Kinetics and thermodynamics across single-file pores: solute permeability and rectified osmosis. *J. Chem. Phys.* 110:606–15

Cruz-Chú ER, Papadopoulou E, Walther JH, Popadić A, Li G, et al. 2017. On phonons and water flow enhancement in carbon nanotubes. *Nat. Nanotechnol.* 12:1106–8

Dagan Z, Weinbaum S, Pfeffer R. 1982. An infinite-series solution for the creeping motion through an orifice of finite length. *J. Fluid Mech.* 115:505–23

Daldrop JO, Kowalik BG, Netz RR. 2017. External potential modifies friction of molecular solutes in water. *Phys. Rev. X* 7:041065

Dekker C. 2007. Solid-state nanopores. *Nat. Nanotechnol.* 2:209–15

Detcheverry F, Bocquet L. 2012. Thermal fluctuations in nanofluidic transport. *Phys. Rev. Lett.* 109:024501

Detcheverry F, Bocquet L. 2013. Thermal fluctuations of hydrodynamic flows in nanochannels. *Phys. Rev. E* 88:012106

Eijkel JC, van den Berg A. 2005. Nanofluidics: What is it and what can we expect from it? *Microfluid. Nanofluid.* 1:249–67

Epsztein R, Shaulsky E, Qin M, Elimelech M. 2019. Activation behavior for ion permeation in ion-exchange membranes: role of ion dehydration in selective transport. *J. Membr. Sci.* 580:316–26

Falk K, Coasne B, Pellenq R, Ulm FJ, Bocquet L. 2015. Subcontinuum mass transport of condensed hydrocarbons in nanoporous media. *Nat. Commun.* 6:6949
Falk K, Sedlmeier F, Joly L, Netz RR, Bocquet L. 2010. Molecular origin of fast water transport in carbon nanotube membranes: superlubricity versus curvature dependent friction. *Nano Lett.* 10:4067–73
Faucher S, Aluru N, Bazant MZ, Blankschtein D, Brozena AH, et al. 2019. Critical knowledge gaps in mass transport through single-digit nanopores: a review and perspective. *J. Phys. Chem. C* 123:21309–26
Feng J, Graf M, Liu K, Ovchinnikov D, Dumcenco D, et al. 2016a. Single-layer MoS_2 nanopores as nanopower generators. *Nature* 536:197–200
Feng J, Liu K, Graf M, Dumcenco D, Kis A, et al. 2016b. Observation of ionic Coulomb blockade in nanopores. *Nat. Mater.* 15:850–55
Feng J, Liu K, Graf M, Lihter M, Bulushev RD, et al. 2015. Electrochemical reaction in single layer MoS_2: nanopores opened atom by atom. *Nano Lett.* 15:3431–38
Finkelstein A. 1987. *Water Movement Through Lipid Bilayers, Pores, and Plasma Membranes*. New York: Wiley
Fouad AM, Gawlinski ET. 2017. Anomalous and nonanomalous behaviors of single-file dynamics. *Phys. Lett. A* 381:2906–11
Fox RF, Uhlenbeck GE. 1970. Contributions to non-equilibrium thermodynamics. I. Theory of hydrodynamical fluctuations. *Phys. Fluids* 13:1893–902
Fumagalli L, Esfandiar A, Fabregas R, Hu S, Ares P, et al. 2018. Anomalously low dielectric constant of confined water. *Science* 360:1339–42
Futamura R, Iiyama T, Takasaki Y, Gogotsi Y, Biggs MJ, et al. 2017. Partial breaking of the Coulombic ordering of ionic liquids confined in carbon nanopores. *Nat. Mater.* 16:1225–32
Garaj S, Hubbard W, Reina A, Kong J, Branton D, Golovchenko JA. 2010. Graphene as a subnanometre trans-electrode membrane. *Nature* 467:190–93
Ghosh S, Sood AK, Kumar N. 2003. Carbon nanotube flow sensors. *Science* 299:1042–44
Gopinadhan K, Hu S, Esfandiar A, Lozada-Hidalgo M, Wang FC, et al. 2019. Complete steric exclusion of ions and proton transport through confined monolayer water. *Science* 363:145–48
Gravelle S, Joly L, Detcheverry F, Ybert C, Cottin-Bizonne C, Bocquet L. 2013. Optimizing water permeability through the hourglass shape of aquaporins. *PNAS* 110:16367–72
Gravelle S, Netz RR, Bocquet L. 2019. Adsorption kinetics in open nanopores as a source of low-frequency noise. *Nano Lett.* 19:7265–72
Gravelle S, Ybert C, Bocquet L, Joly L. 2016. Anomalous capillary filling and wettability reversal in nanochannels. *Phys. Rev. E* 93:033123
Grosjean B, Bocquet ML, Vuilleumier R. 2019. Versatile electrification of two-dimensional nanomaterials in water. *Nat. Commun.* 10:1656
Hall JE. 1975. Access resistance of a small circular pore. *J. Gen. Physiol.* 66:531–32
Hauge EH, Martin-Lof A. 1973. Fluctuating hydrodynamics and Brownian motion. *J. Stat. Phys.* 7:259–81
Hille B. 1968. Pharmacological modifications of the sodium channels of frog nerve. *J. Gen. Physiol.* 51:199–219
Holt JK, Park HG, Wang Y, Stadermann M, Artyukhin AB, et al. 2006. Fast mass transport through sub-2-nanometer carbon nanotubes. *Science* 312:1034–37
Hooge FN. 1969. $1/f$ noise is no surface effect. *Phys. Lett. A* 29:139–40
Hoogerheide DP, Garaj S, Golovchenko JA. 2009. Probing surface charge fluctuations with solid-state nanopores. *Phys. Rev. Lett.* 102:5–8
Horner A, Pohl P. 2018a. Comment on "Enhanced water permeability and tunable ion selectivity in subnanometer carbon nanotube porins." *Science* 359:eaap9173
Horner A, Pohl P. 2018b. Single-file transport of water through membrane channels. *Faraday Discuss.* 209:9–33
Horner A, Zocher F, Preiner J, Ollinger N, Siligan C, et al. 2015. The mobility of single-file water molecules is governed by the number of H-bonds they may form with channel-lining residues. *Sci. Adv.* 1:e1400083
Hummer G, Rasaiah JC, Noworyta JP. 2001. Water conduction through the hydrophobic channel of a carbon nanotube. *Nature* 414:188–90
Israelachvili JN. 2011. Electrostatic forces between surfaces in liquids. In *Intermolecular and Surface Forces*, pp. 291–340. Burlington, MA: Academic. 3rd ed.
Israelachvili JN, Pashley RM. 1983. Molecular layering of water at surfaces and origin of repulsive hydration forces. *Nature* 306:249–50

Jain T, Rasera BC, Guerrero RJS, Boutilier MS, O'Hern SC, et al. 2015. Heterogeneous sub-continuum ionic transport in statistically isolated graphene nanopores. *Nat. Nanotechnol.* 10:1053–57
Kaiser V, Bramwell ST, Holdsworth PC, Moessner R. 2013. Onsager's Wien effect on a lattice. *Nat. Mater.* 12:1033–37
Kalra A, Garde S, Hummer G. 2003. Osmotic water transport through carbon nanotube membranes. *PNAS* 100:10175–80
Kappler J, Daldrop JO, Brünig FN, Boehle MD, Netz RR. 2018. Memory-induced acceleration and slowdown of barrier crossing. *J. Chem. Phys.* 148:014903
Kaufman IK, McClintock PV, Eisenberg RS. 2015. Coulomb blockade model of permeation and selectivity in biological ion channels. *New J. Phys.* 17:083021
Kavokine N, Marbach S, Siria A, Bocquet L. 2019. Ionic Coulomb blockade as a fractional Wien effect. *Nat. Nanotechnol.* 14:573–78
Keerthi A, Geim AK, Janardanan A, Rooney AP, Esfandiar A, et al. 2018. Ballistic molecular transport through two-dimensional channels. *Nature* 558:420–23
Keyser UF, Koeleman BN, van Dorp S, Krapf D, Smeets RM, et al. 2006. Direct force measurements on DNA in a solid-state nanopore. *Nat. Phys.* 2:473–77
Khair AS, Squires TM. 2008. Surprising consequences of ion conservation in electro-osmosis over a surface charge discontinuity. *J. Fluid Mech.* 615:323–34
Knudsen M. 1909. Die Gesetze der Molekularströmung und der inneren Reibungsströmung der Gase durch Röhren. *Ann. Phys.* 333:75–130
Koenig SP, Wang L, Pellegrino J, Bunch JS. 2012. Selective molecular sieving through porous graphene. *Nat. Nanotechnol.* 7:728–32
Köfinger J, Hummer G, Dellago C. 2011. Single-file water in nanopores. *Phys. Chem. Chem. Phys.* 13:15403–17
Kondrat S, Kornyshev A. 2011. Superionic state in double-layer capacitors with nanoporous electrodes. *J. Phys. Condens. Matter* 23:022201
Kralchevsky PA, Denkov ND. 1995. Analytical expression for the oscillatory structural surface force. *Chem. Phys. Lett.* 240:385–92
Landau L, Lifshitz E. 1977. IX. Hydrodynamic fluctuations. In *Statistical Physics: Part 2*, pp. 360–84. Elmsford, NY: Pergamon
Lauga E, Brenner M, Stone H. 2007. Microfluidics: the no-slip boundary condition. In *Springer Handbook of Experimental Fluid Mechanics*, ed. C Tropea, AL Yarin, JF Foss, pp. 1219–40. Berlin: Springer-Verlag
Lee AA, Kondrat S, Kornyshev AA. 2014. Single-file charge storage in conducting nanopores. *Phys. Rev. Lett.* 113:048701
Lee C, Joly L, Siria A, Biance AL, Fulcrand R, Bocquet L. 2012. Large apparent electric size of solid-state nanopores due to spatially extended surface conduction. *Nano Lett.* 12:4037–44
Lee CY, Choi W, Han JH, Strano MS. 2010. Coherence resonance in a single-walled carbon nanotube ion channel. *Science* 329:1320–24
Lee J, Laoui T, Karnik R. 2014. Nanofluidic transport governed by the liquid/vapour interface. *Nat. Nanotechnol.* 9:317–23
Lei W, Rigozzi MK, McKenzie DR. 2016. The physics of confined flow and its application to water leaks, water permeation and water nanoflows: a review. *Rep. Prog. Phys.* 79:025901
Levin Y. 2002. Electrostatic correlations: from plasma to biology. *Rep. Prog. Phys.* 65:1577–632
Levin Y. 2006. Electrostatics of ions inside the nanopores and trans-membrane channels. *Europhys. Lett.* 76:163–69
Levine S, Marriott JR, Robinson K. 1975. Theory of electrokinetic flow in a narrow parallel-plate channel. *J. Chem. Soc. Faraday Trans. 2* 71:1–11
Levitt DG. 1973. Dynamics of a single-file pore: non-Fickian behavior. *Phys. Rev. A* 8:3050–54
Levy A, Pedro de Souza J, Bazant M. 2020. Breakdown of electroneutrality in nanopores. arXiv:1905.05789 [cond-mat.soft]
Li W, Wang W, Zhang Y, Yan Y, Dai C, Zhang J. 2017. Gated water transport through graphene nanochannels: from ionic coulomb blockade to electroosmotic pump. *J. Phys. Chem. C* 121:17523–29
Liu H, He J, Tang J, Liu H, Pang P, et al. 2010. Translocation of single-stranded DNA through single-walled carbon nanotubes. *Science* 327:64–67

Liu L, Yang C, Zhao K, Li J, Wu HC. 2013. Ultrashort single-walled carbon nanotubes in a lipid bilayer as a new nanopore sensor. *Nat. Commun.* 4:2989

Loche P, Ayaz C, Schlaich A, Uematsu Y, Netz RR. 2019. Giant axial dielectric response in water-filled nanotubes an effective electrostatic ion–ion interactions from a tensorial dielectric model. *J. Phys. Chem. B* 123:10850–57

Ma M, Grey F, Shen L, Urbakh M, Wu S, et al. 2015. Water transport inside carbon nanotubes mediated by phonon-induced oscillating friction. *Nat. Nanotechnol.* 10:692–95

MacKinnon R. 2004. Potassium channels and the atomic basis of selective ion conduction. *Biosci. Rep.* 24:75–100

Maduar SR, Belyaev AV, Lobaskin V, Vinogradova OI. 2015. Electrohydrodynamics near hydrophobic surfaces. *Phys. Rev. Lett.* 114:118301

Mahan G. 2000. Homogeneous electron gas. In *Many-Particle Physics*, pp. 295–374. New York: Springer. 3rd ed.

Majumder M, Smalley RE, Hinds BJ. 2008. *Mass transport through carbon nanotube membranes in three different regimes: ionic, liquid and gas*. Paper presented at the AIChE 2008 Annual Meeting, Philadelphia, PA, Nov. 18

Malgaretti P, Pagonabarraga I, Rubi JM. 2014. Entropic electrokinetics: recirculation, particle separation, and negative mobility. *Phys. Rev. Lett.* 113:128301

Mamatkulov SI, Allolio C, Netz RR, Bonthuis DJ. 2017. Orientation-induced adsorption of hydrated protons at the air–water interface. *Angew. Chem. Int. Ed.* 56:15846–51

Manghi M, Palmeri J, Yazda K, Henn F, Jourdain V. 2018. Role of charge regulation and flow slip in the ionic conductance of nanopores: an analytical approach. *Phys. Rev. E* 98:012605

Marbach S, Dean DS, Bocquet L. 2018. Transport and dispersion across wiggling nanopores. *Nat. Phys.* 14:1108–13

Marcotte A, Mouterde T, Niguès A, Siria A, Bocquet L. 2020. Mechanically activated ionic transport across single-digit carbon nanotubes. *Nat. Mater.* 19:1057–61

Mashiyama KT, Mori H. 1978. Origin of the Landau-Lifshitz hydrodynamic fluctuations in nonequilibrium systems and a new method for reducing the Boltzmann equation. *J. Stat. Phys.* 18:385–407

Merlet C, Rotenberg B, Madden PA, Taberna PL, Simon P, et al. 2012. On the molecular origin of supercapacitance in nanoporous carbon electrodes. *Nat. Mater.* 11:306–10

Misra RP, Blankschtein D. 2017. Insights on the role of many-body polarization effects in the wetting of graphitic surfaces by water. *J. Phys. Chem. C* 121:28166–79

Mouhat F, Coudert FX, Bocquet ML. 2020. Structure and chemistry of graphene oxide in liquid water from first principles. *Nat. Commun.* 11:1566

Mouterde T, Bocquet L. 2018. Interfacial transport with mobile surface charges and consequences for ionic transport in carbon nanotubes. *Eur. Phys. J. E* 41:148

Mouterde T, Keerthi A, Poggioli AR, Dar SA, Siria A, et al. 2019. Molecular streaming and its voltage control in ångström-scale channels. *Nature* 567:87–90

Murata K, Mitsuoka K, Hiral T, Walz T, Agre P, et al. 2000. Structural determinants of water permeation through aquaporin-1. *Nature* 407:599–605

Neek-Amal M, Lohrasebi A, Mousaei M, Shayeganfar F, Radha B, Peeters FM. 2018. Fast water flow through graphene nanocapillaries: a continuum model approach involving the microscopic structure of confined water. *Appl. Phys. Lett.* 113:083101

Neek-Amal M, Peeters FM, Grigorieva IV, Geim AK. 2016. Commensurability effects in viscosity of nanoconfined water. *ACS Nano* 10:3685–92

Nicholson D, Quirke N. 2003. Ion pairing in confined electrolytes. *Mol. Simul.* 29:287–90

O'Hern SC, Stewart CA, Boutilier MS, Idrobo JC, Bhaviripudi S, et al. 2012. Selective molecular transport through intrinsic defects in a single layer of CVD graphene. *ACS Nano* 6:10130–38

Onsager L. 1934. Deviations from Ohm's law in weak electrolytes. *J. Chem. Phys.* 2:599–615

Pang P, He J, Park JH, Krstić PS, Lindsay S. 2011. Origin of giant ionic currents in carbon nanotube channels. *ACS Nano* 5:7277–83

Parsegian A. 1969. Energy of an ion crossing a low dielectric membrane: solutions to four relevant electrostatic problems. *Nature* 221:844–46

Perram JW, Hunter RJ, Wright HJ. 1973. Charge and potential at the oxide/solution interface. *Chem. Phys. Lett.* 23:265–69

Portella G, Pohl P, De Groot BL. 2007. Invariance of single-file water mobility in gramicidin-like peptidic pores as function of pore length. *Biophys. J.* 92:3930–37

Rabinowitz J, Cohen C, Shepard KL. 2020. An electrically actuated, carbon-nanotube-based biomimetic ion pump. *Nano Lett.* 20(2):1148–53

Radha B, Esfandiar A, Wang FC, Rooney AP, Gopinadhan K, et al. 2016. Molecular transport through capillaries made with atomic-scale precision. *Nature* 538:222–25

Reguera D, Rubí JM. 2001. Kinetic equations for diffusion in the presence of entropic barriers. *Phys. Rev. E* 64:061106

Renkin EM. 1954. Filtration, diffusion, and molecular sieving through porous cellulose membranes. *J. Gen. Physiol.* 38:225–43

Richards LA, Schäfer AI, Richards BS, Corry B. 2012. The importance of dehydration in determining ion transport in narrow pores. *Small* 8:1701–9

Sahu S, Zwolak M. 2019. Ionic phenomena in nanoscale pores through 2D materials. *Rev. Mod. Phys.* 91:021004

Sampson R. 1891. On Stokes's current function. *Philos. Trans. R. Soc. Lond.* 182:449–518

Saparov SM, Pfeifer JR, Al-Momani L, Portella G, De Groot BL, et al. 2006. Mobility of a one-dimensional confined file of water molecules as a function of file length. *Phys. Rev. Lett.* 96:148101

Schlaich A, Kappler J, Netz RR. 2017. Hydration friction in nanoconfinement: from bulk via interfacial to dry friction. *Nano Lett.* 17:5969–75

Schlaich A, Knapp EW, Netz RR. 2016. Water dielectric effects in planar confinement. *Phys. Rev. Lett.* 117:048001

Schoch RB, Han J, Renaud P. 2008. Transport phenomena in nanofluidics. *Rev. Mod. Phys.* 80:839–83

Secchi E, Marbach S, Niguès A, Stein D, Siria A, Bocquet L. 2016a. Massive radius-dependent flow slippage in carbon nanotubes. *Nature* 537:210–13

Secchi E, Niguès A, Jubin L, Siria A, Bocquet L. 2016b. Scaling behavior for ionic transport and its fluctuations in individual carbon nanotubes. *Phys. Rev. Lett.* 116:154501

Silkina EF, Asmolov ES, Vinogradova OI. 2019. Electro-osmotic flow in hydrophobic nanochannels. *Phys. Chem. Chem. Phys.* 21:23036–43

Siria A, Poncharal P, Biance AL, Fulcrand R, Blase X, et al. 2013. Giant osmotic energy conversion measured in a single transmembrane boron nitride nanotube. *Nature* 494:455–58

Siwy Z, Fuliński A. 2002. Origin of $1/f^{\alpha}$ noise in membrane channel currents. *Phys. Rev. Lett.* 89:158101

Smeets RMM, Keyser UF, Dekker NH, Dekker C. 2008. Noise in solid-state nanopores. *PNAS* 105:417–21

Smoluchowski M. 1910. Zur kinetischen Theorie der Transpiration und Diffusion verdünnter Gase. *Ann. Phys.* 338:1559–70

Sparreboom W, van den Berg A, Eijkel JC. 2010. Transport in nanofluidic systems: a review of theory and applications. *New J. Phys.* 12:015004

Steckelmacher W. 1966. A review of the molecular flow conductance for systems of tubes and components and the measurement of pumping speed. *Vacuum* 16:561–84

Tasserit C, Koutsioubas A, Lairez D, Zalczer G, Clochard MC. 2010. Pink noise of ionic conductance through single artificial nanopores revisited. *Phys. Rev. Lett.* 105:260602

Taylor G. 1953. Dispersion of soluble matter in solvent flowing slowly through a tube. *Proc. R. Soc. A* 219:186–203

Teber S. 2005. Translocation energy of ions in nano-channels of cell membranes. *J. Stat. Mech. Theory Exp.* 2005:P07001

Thomas JA, McGaughey AJ. 2009. Water flow in carbon nanotubes: transition to subcontinuum transport. *Phys. Rev. Lett.* 102:184502

Travis KP, Todd BD, Evans DJ. 1997. Departure from Navier-Stokes hydrodynamics in confined liquids. *Phys. Rev. E* 55:4288–95

Tunuguntla RH, Henley RY, Yao YC, Pham TA, Wanunu M, Noy A. 2017. Enhanced water permeability and tunable ion selectivity in subnanometer carbon nanotube porins. *Science* 357:792–96

Tunuguntla RH, Zhang Y, Henley RY, Yao YC, Pham TA, et al. 2018. Response to Comment on "Enhanced water permeability and tunable ion selectivity in subnanometer carbon nanotube porins." *Science* 359:eaaq1241

Uematsu Y, Bonthuis DJ, Netz RR. 2019. Impurity effects at hydrophobic surfaces. *Curr. Opin. Electrochem.* 13:166–73

Uematsu Y, Netz RR, Bocquet L, Bonthuis DJ. 2018. Crossover of the power-law exponent for carbon nanotube conductivity as a function of salinity. *J. Phys. Chem. B* 122:2992–97

Vlassiouk I, Siwy ZS. 2007. Nanofluidic diode. *Nano Lett.* 7:552–56

Walker MI, Ubych K, Saraswat V, Chalklen EA, Braeuninger-Weimer P, et al. 2017. Extrinsic cation selectivity of 2D membranes. *ACS Nano* 11:1340–46

Weissberg HL. 1962. End correction for slow viscous flow through long tubes. *Phys. Fluids* 5:1033

Wohnsland F, Benz R. 1997. $1/f$-Noise of open bacterial porin channels. *J. Membr. Biol.* 158:77–85

Won CY, Aluru NR. 2007. Water permeation through a subnanometer boron nitride nanotube. *J. Am. Chem. Soc.* 129:2748–49

Wu J, Lewis AH, Grandl J. 2017. Touch, tension, and transduction—the function and regulation of Piezo ion channels. *Trends Biochem. Sci.* 42:57–71

Xie Y, Fu L, Niehaus T, Joly L. 2020. Liquid-solid slip on charged walls: the dramatic impact of charge distribution. *Phys. Rev. Lett.* 125:014501

Yazda K, Tahir S, Michel T, Loubet B, Manghi M, et al. 2017. Voltage-activated transport of ions through single-walled carbon nanotubes. *Nanoscale* 9:11976–86

Zhang C, Gygi F, Galli G. 2013. Strongly anisotropic dielectric relaxation of water at the nanoscale. *J. Phys. Chem. Lett.* 4:2477–81

Zhang J, Kamenev A, Shklovskii BI. 2006. Ion exchange phase transitions in water-filled channels with charged walls. *Phys. Rev. E* 73:051205

Zhang J, Todd BD, Travis KP. 2004. Viscosity of confined inhomogeneous nonequilibrium fluids. *J. Chem. Phys.* 121:10778–86

Zhu F, Tajkhorshid E, Schulten K. 2004. Collective diffusion model for water permeation through microscopic channels. *Phys. Rev. Lett.* 93:224501

Zorkot M, Golestanian R, Bonthuis DJ. 2016. The power spectrum of ionic nanopore currents: the role of ion correlations. *Nano Lett.* 16:2205–12